

# Conceptual Study on Robust Rebound Suppression Mechanism for Small-Body Landing

Kikuko Miyata<sup>\*</sup>, Manato Nozaki<sup>†</sup>, Susumu Hara<sup>‡</sup>, and Kohei Yamaguchi<sup>§</sup>  
*Nagoya University, Nagoya, 464-8603, Japan*

Masatsugu Otsuki<sup>¶</sup>  
*Japan Aerospace Exploration Agency, Sagamihara, 252-5210, Japan*

Landing on celestial bodies typically includes a free fall to the body surface and requires energy dissipation. Landing sites can exhibit many uncertainties, especially in surface parameters. Therefore, robustness is required irrespective of variations in landing conditions. Conventional mechanisms, such as shock absorbers or airbags, have repeatedly achieved safe landings; however, they are not reusable in the ground-verification phase and cause complexity. In this study, we propose a robust, lightweight, and simple rebound suppression mechanism with reusability in the ground verification phase by simultaneously considering the characteristics of mechanical energy and momentum exchange aspects. The design characteristics are clarified mainly through numerical discussions, and the effectiveness of the proposed mechanism is demonstrated in comparison to existing momentum exchange mechanisms. The results show a promising rebound suppression capability compared to those of the previously suggested mechanisms and an improvement in robustness against uncertainties. A case study is also shown to verify the proposed mechanism's effectiveness. Numerical simulation results for a fictional landing mission created from real microgravity landers show that the proposed mechanism achieves the energy dissipation requirement, combined with the plastic deformation mechanism of the shock-absorbing material.

## I. Nomenclature

$a$	=	compression of the spring, m
$c_f$	=	ground viscosity, kN·s/m
$c_g$	=	viscous friction of the linear guide, N·s/m

---

<sup>\*</sup> Assistant Professor, Department of Aerospace Engineering, Graduate School of Engineering, Furo-cho, Chikusa-ku, Aichi, and AIAA Member.

<sup>†</sup> Graduate Student, Department of Aerospace Engineering, Graduate School of Engineering, Furo-cho, Chikusa-ku, Aichi

<sup>‡</sup> Professor, Department of Aerospace Engineering, Graduate School of Engineering, Furo-cho, Chikusa-ku, Aichi, and AIAA Senior Member.

<sup>§</sup> Assistant Professor, Department of Aerospace Engineering, Graduate School of Engineering, Furo-cho, Chikusa-ku, Aichi

<sup>¶</sup> Associate Professor, Department of Spacecraft Engineering, Institute of Space and Astronautical Science, Japan Aerospace Exploration Agency, Chuo-ku, Kanagawa.

$f_g$	=	mechanical loss, N
$g$	=	gravitational acceleration, m/s <sup>2</sup>
$h_0$	=	initial altitude, m
$k$	=	spring constant, N/m
$k_f$	=	ground stiffness, N/m
$l$	=	natural length of the spring, m
$m_1, m_2$	=	spacecraft and additional mass, kg
$p, A, B$	=	constants
$t_0$	=	spring release time, s
$v_0$	=	initial velocity, m/s
$x_1, x_2$	=	spacecraft and additional mass displacement, m
$\ddot{x}_1, \ddot{x}_2$	=	spacecraft and additional mass acceleration, m/s <sup>2</sup>
$\dot{x}_1, \dot{x}_2$	=	spacecraft and additional mass velocity, m/s
$\omega$	=	angular frequency, rad/s

## II. Introduction

Recently, small body investigations have gained popularity owing to their importance in understanding the early history and evolution of the solar system [1–8]. Two main methods are used to observe celestial bodies; remote sensing from orbits and direct observation by landing. The former can achieve a relatively large-scale observation, whereas the latter provides extracting fine details of celestial bodies over a limited area, such as the composition of their soil. On the other hand, many challenges exist to achieve landing on the ground for the latter method. Usually, mission success depends on safe landing, which is only a one-time opportunity. Therefore, a highly reliable landing mechanism is required that endures the uncertainties of the landing environment. Celestial bodies tend to be covered with regolith, which may affect on-board electronics [9]. In the case of a spacecraft landing on such a ground, free-falling from a certain altitude is commonly used [10]. A free fall without a thruster jet avoids sample contamination and regolith disturbance [11]. Earlier studies have investigated the mitigation of shock energy during landing by considering the acceleration caused by free-falling [10, 12–17].

Rebound suppression is one of the most important criteria to achieve precise landing to the target point [18] and prevent overturning [19]. However, determining ground characteristics of important exploration sites, such as asteroids or comets, during the design of the landing system is a challenge [20]. Therefore, developing a robust landing technique is required for the unknown surface parameters of the landing points. Moreover, an increase in spacecraft mass reduces launch capability; hence, severe mass constraints are imposed on the spacecraft [21]. Thus, highly reliable and

lightweight landing mechanisms, which can reduce rebound to the target point with arbitrary surface properties, are required for direct celestial body observations.

For microgravity celestial bodies such as asteroids the same landing impact energy causes a higher rebound than that for lunar or planetary missions. Therefore, efficient energy dissipation for rebound prevention is desired. Anchoring is often required to prevent re-bouncing [22]. For example, Philae [18, 22] successfully landed on a comet '67P/Churyumov Gerasimenko' in 2014. Its energy-absorbing damping system had been designed to achieve robust and rebound-less landing. Although the system achieved more than 90% energy dissipation, an unexpected failure in the landing sequence caused bouncing, causing it to tip over and partial achievement of the mission [23]. Another example is an upcoming mission to land on the Martian satellite Phobos in 2024 [24], whose gravity is 1/2000 of the Earth; therefore, suppressing the kinetic energy to prevent rebound becomes critical. In Ref. [11], they say "A trip-over risk remains unless the landing system consumes more than 99 percent of the entire kinetic energy." The rebound can cause unstable motions under the microgravity environment [25]. Thus, landing on a microgravity celestial body without tipping over is very difficult. Even a small fraction of the remaining energy can cause rebound under microgravity environment, and trigger unexpected events. In this work, we discuss the rebound suppression problem for landing on microgravity celestial bodies and propose a novel mechanism for this purpose.

As explained before, the landing mechanisms must be lightweight and have highly reliable rebound suppression capability. Additionally, a robust landing technique is required to endure unknown surface properties. Landing on microgravity celestial bodies has different characteristics compared to landing on a planet or large moon; however, many proven methods have been developed [26]. Conventional landing mechanisms are divided into passive and active methods. Shock absorbers [27] and airbags [28–32] have been used as passive methods, while reverse thrust systems [33–35] or sky crane mechanisms [36–39] are popular for active methods.

A landing mechanism such as the honeycomb crash mechanism dissipates the kinetic energy through plastic deformation and realizes soft landing [27]. The advantages of these mechanisms are their lightweight and high energy absorption. However, the mechanism encounters challenges against rough terrains, such as hills or slopes. In addition, these mechanisms are disposable, meaning that precisely performing preliminary operational inspection is difficult; thus, it is impossible to precisely verify the targeted product through the ground test. Manufacturer verification requires expensive lot tests of the product with the same design to ensure reliability. Although their mechanisms are simple, their reliability is low compared with the mechanism that can perform product-specific tests. An airbag is suitable for small satellites [28–32] due to lightweight, low cost, and high reliability. Although a typical airbag can reduce energy, it cannot suppress the rebound. Therefore, it is unsuitable for the missions that require accurate landing on inclined terrains. The rebound can be suppressed by controlling the open status of the vent holes; however, it increases the complexity of the system [40]. Reverse thrust system [33–35] descends the altitude using propulsion systems. A sky crane [36–39] is a landing method that hangs the lander from a floating stage using reverse thrust and gradually

descends the lander. These methods can achieve precise landing and provide adjustments for surface conditions due to their active control aspect. However, they require sophisticated control to maintain position and velocity, causing an increase in mass.

Therefore, the state-of-the-art mechanisms do not satisfy all the requirements, which include rebound suppression, robust landing despite arbitrary ground parameters, lightweight, high reliability, and low cost. Thus, proposed landing mechanisms that enable uncomplicated and precise landing with a straightforward control system have been proposed, such as the base extension separation mechanism (BESM) [12] and momentum exchange impact damper (MEID) [13].

The BESM relies on the concept of dynamic energy conversion (Fig. 1). This mechanism absorbs the landing impact energy by converting it into the potential energy of the spring and removes the mechanical energy by separating the additional mass from the main body, and the additional mass when the spring is most contracted. However, this mechanism is complicated, and the timing of detachment depends on the nature of the ground. As shown in Fig. 1, the sequence starts with a free fall. After the gear touchdown, the spring is stretched, and energy is transferred to the spring elastic energy. Then, the additional mass locking device opens when the spring stretches at maximum. Finally, the additional mass is released, and thus, the main body can land softly because most of the energy is transferred to the additional mass.

The MEID mechanism realizes rebound suppression by attaching a spring and an additional mass to the spacecraft body and transfers the momentum of the spacecraft body to the additional mass. The mechanism was first proposed to solve the floor impact vibration [41]. It was then applied to the spacecraft landing problem for conceptual laboratory investigations [14]. The proposed MEID mechanisms vary based on spring state and injection direction as shown in Fig. 2. The Upper MEID (U-MEID) achieves the momentum exchange and rebound suppression by launching the upper additional mass upward as a response to the landing. Its spring is initially in the natural state [15]. The Lower MEID (L-MEID) achieves the momentum exchange and soft landing by releasing of the lower additional mass downward before landing. The spring is initially pre-compressed and additional mass release occurs when the spring reaches its natural length the first time [14]. The Generalized MEID (G-MEID) mechanism has the properties of both U-MEID and L-MEID and uses a combination of lower and upper additional masses. The momentum exchange sequence starts with the separation of the lower mass [16]. The Generalized MEID Advanced (G-MEID-A) mechanism performs function of the G-MEID mechanism only with an upper additional mass with an extended spring [17]. The G-MEID-A mechanism shows the best rebound suppression capability among these methods. However, it requires strict timing control for spring release and the error causes critical performance reduction. The timing of spring release is related to rebound conditions caused by the celestial body surface. Therefore, the mechanism falls short of delivering soft landing on an unknown celestial surface.

Therefore, we propose a novel MEID mechanism by simultaneously considering the characteristics of mechanical energy and momentum exchange aspects. Specifically, our proposed mechanism comprises two phases: Phase A

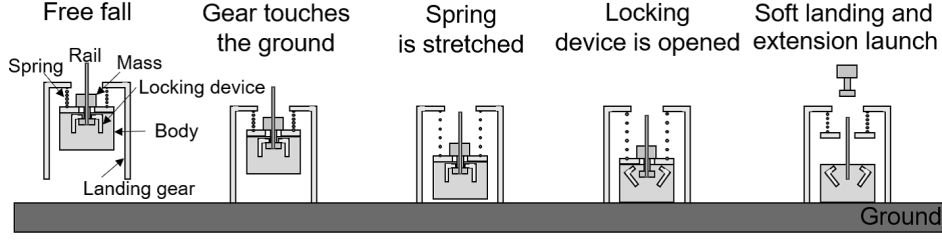


**Fig. 1 Concept of the BESM (base extension separation mechanism).**

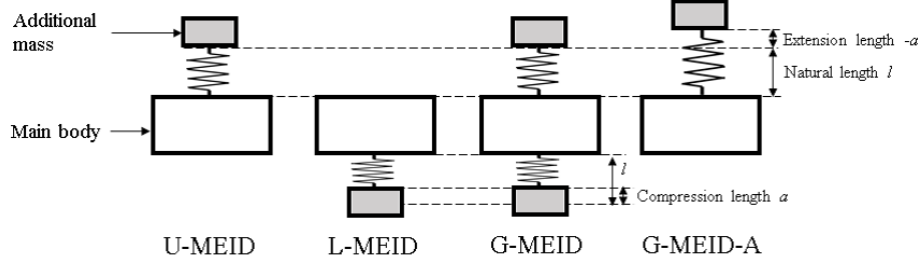


**Fig. 2 Configuration and initial conditions of MEID (momentum exchange impact damper).**

achieves the energy transfer, as in BESM, and Phase B performs momentum exchange, as achieved by MEID. In Phase A, a detailed analysis of the energy exchange is considered, especially the timing, amount, and duration of the elastic energy of the spring. The characteristics of the proposed mechanism are discussed through numerical analysis and in comparison to previous MEID mechanisms. An experimental study is also demonstrated and compared to numerical analysis results. In addition, a case study is employed to discuss the application prospects of the proposed mechanism. The MEID mechanism has not yet been applied in a real flight mission; however, our results show that the proposed mechanism can be realized in a future mission. Based on the MEID utilization of the proposed mechanism, the shock response performance becomes larger as the additional mass rate becomes higher. Therefore, the proposed system offers advantages for a very tiny lander; for example, it is very difficult to mount a thruster tank because there are certain volume and mass requirement from structural and safe design constraints, and the required additional mass using the proposed system is lightweight. Generally, realizing mass ejection systems is difficult; however, the lightweight of additional mass can significantly facilitate it. The proposed mechanism offers advantages when it has separation mission equipment such as a tiny lander or outer camera.

The rest of the paper is organized as follows: Section III proposes a novel MEID mechanism to provide the robustness against ground parameter uncertainties. Additionally, the details of the proposed mechanism are explained by constructing a numerical simulation model. Section IV summarizes the numerical simulation results, including design parameter optimization, and the robustness against the uncertainties of the landing parameters. The results are discussed by comparing with those obtained using the G-MEID-A mechanism, which shows the best rebound

suppression performances among the previous MEID systems. The lunar landing problem is applied to the simulation conditions since the correlations between the numerical simulation and real motion have been demonstrated. Section V shows the experimental simulation results. The results of the previous studies clarify the relationship between ground and lunar surface experiments. Ground experiments were performed with the experimental system emulating the lunar surface conditions. The numerical simulation results were compared with the experimental simulation results. The unknown mechanical parameters in the numerical model were determined by a comparison of the numerical and experimental simulation results. Section VI shows a case study utilizing the proposed mechanism with the help of the established numerical models. The proposed mechanism applies to lightweight landers under microgravity environments. Landing on the Martian satellite Phobos requires strict rebound suppression. Therefore, it is set as the landing target body for numerical simulation studies.

### III. Proposed mechanism

#### A. Concept of the proposed mechanism

This paper proposes a new landing impulse response control inspired by the two properties of the momentum exchange and mechanical energy exchange as one option for the future mission. The effectiveness and feasibility of the proposed concept are discussed by utilizing a simplified mechanical model, which consists of the main spacecraft body, spring, and additional mass. Figure 3 shows an overview of the optimum landing sequence of the proposed mechanism. The gray and white boxes express the additional mass and main spacecraft body, respectively, and they are connected by the spring. The black arrows express the force. This mechanism achieves soft landing in the following sequence:

- 1) The additional mass is fixed to the upper end of the spacecraft main body with a pre-compressed spring. The spring has stored elastic energy at the beginning of the free fall at time  $t = 0$ .
- 2) With the spring compression release at the designed time  $t = t_0$ , the additional mass has an upward acceleration, and the spacecraft main body has a downward acceleration.
- 3) The main body lands on the ground when the spring extends to the maximum length  $t = t_1$ . At the time of the landing, the spring connecting the spacecraft main body and additional mass is elongated, the upward acceleration is generated in the spacecraft body, and the collision acceleration can be decreased because of the reduction in the kinetic energy of the spacecraft main body.
- 4) The extended spring is contracted by exchanging part of the impact energy of the landing.
- 5) The stored elastic energy is exchanged with the kinetic energy of the additional mass. The additional mass is injected by spring separation when the spring is in the natural state. The main body's momentum is exchanged

with additional mass momentum.

Sequences 1 to 4 achieve the mechanical energy exchange similar to the BESM mechanism, although there is no locking device. Sequence 5 achieves the momentum exchange, such as the existing MEID mechanisms. The proposed system combines the advantages of both mechanisms. The soft landing and rebound suppression are realized through both aspects. The upward acceleration of the main body generated at the landing time reduces the effect of the timing error and realizes the robustness against various uncertainties. In this work, we construct and analyze system models and verify the effectiveness of the proposed mechanism through numerical and experimental simulations.

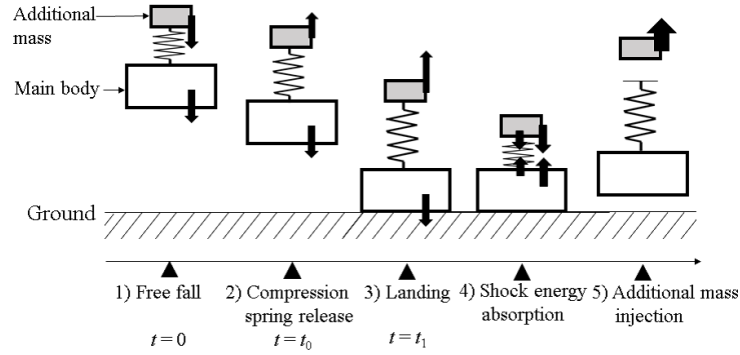


**Fig. 3 Concept of the proposed mechanism.**

## B. Mechanical model and equation of the motion of MEID mechanism

A dynamical model for the proposed mechanism is established to derive equation of motion for the numerical simulation studies. Figure 4 shows the model overview. The spacecraft main body and additional mass are defined as  $m_1$  and  $m_2$ , respectively. The displacement, velocity, and acceleration of the main body and the additional mass are defined as  $x_1, x_2, \dot{x}_1, \dot{x}_2, \ddot{x}_1$ , and  $\ddot{x}_2$ , respectively. The main body and the additional mass are connected with the spring, whose stiffness is denoted as  $k$ . Here, we assume ideal linear spring to provide a conceptual discussion. In reality, we need to also consider nonlinear behavior. The stiffness of the ground is  $k_f$ , and the viscous damping between the spacecraft and ground is  $c_f$ . The initial free-fall altitude from the ground is  $h_0$ . The whole landing motion is divided into four phases.

### Phase 1: Before spring release

The main body of the spacecraft and the additional mass free fall together until the restrained spring is released. Therefore, the equation of motion of Phase 1 is expressed as follows with the gravitational acceleration of  $g$ :

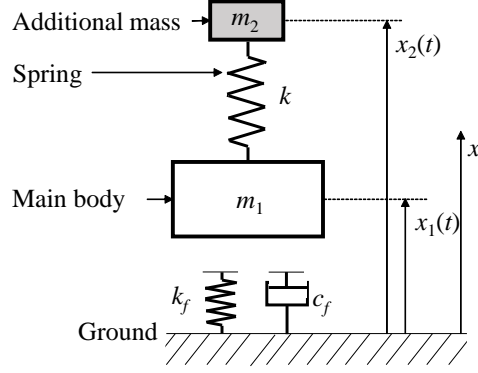


**Fig. 4 Model of the proposed mechanism.**

$$\begin{bmatrix} m_1 & 0 \\ 0 & m_2 \end{bmatrix} \begin{bmatrix} \ddot{x}_1(t) \\ \ddot{x}_2(t) \end{bmatrix} = \begin{bmatrix} -m_1 g \\ -m_2 g \end{bmatrix} \quad (1)$$

Phase 2: From spring release to landing

The main body and additional mass receive the gravitational and reaction forces of the spring that connects them. The equation of motion of Phase 2 is derived from the relationship of the forces as follows when the natural length of the spring is denote as  $l$ :

$$\begin{bmatrix} m_1 & 0 \\ 0 & m_2 \end{bmatrix} \begin{bmatrix} \ddot{x}_1(t) \\ \ddot{x}_2(t) \end{bmatrix} + \begin{bmatrix} k & -k \\ -k & k \end{bmatrix} \begin{bmatrix} x_1(t) \\ x_2(t) \end{bmatrix} = \begin{bmatrix} -m_1 g - kl \\ -m_2 g + kl \end{bmatrix} \quad (2)$$

Phase 3: From landing to additional mass separation

Phase 3 receives the reaction force from the ground in addition to the relationship of Phase 2. The equation of motion of Phase 3 is derived as follows from the relationship of the forces:

$$\begin{bmatrix} m_1 & 0 \\ 0 & m_2 \end{bmatrix} \begin{bmatrix} \ddot{x}_1(t) \\ \ddot{x}_2(t) \end{bmatrix} + \begin{bmatrix} c_f & 0 \\ 0 & 0 \end{bmatrix} \begin{bmatrix} \dot{x}_1(t) \\ \dot{x}_2(t) \end{bmatrix} + \begin{bmatrix} k + k_f & -k \\ -k & k \end{bmatrix} \begin{bmatrix} x_1(t) \\ x_2(t) \end{bmatrix} = \begin{bmatrix} -m_1 g - kl \\ -m_2 g + kl \end{bmatrix} \quad (3)$$

Phase 4: After additional mass separation

After the additional mass separation, the spacecraft's main body and the additional mass only receive gravitational



force. Therefore, the equation of motion of Phase 4 is expressed as follows:

$$\begin{bmatrix} m_1 & 0 \\ 0 & m_2 \end{bmatrix} \begin{bmatrix} \ddot{x}_1(t) \\ \ddot{x}_2(t) \end{bmatrix} = \begin{bmatrix} -m_1 g \\ -m_2 g \end{bmatrix} \quad (4)$$

The time series status of the components can be derived by numerically integrating of these equations. Phase transfers are performed passively depends on the system mechanical parameters, except for the transfer between Phases 1 and 2. The designer can arbitrarily define the phase transfer time  $t_0$  between Phases 1 and 2 arbitrarily.

### C. Optimum design parameter to maximize energy suppression performance

This study investigates the free fall energy dissipation and aims to minimize the spacecraft energy at the time of landing, which can be evaluated with the maximum rebound amount of the spacecraft. After the separation of the additional mass, during Phase 4, each component is only accelerated with the gravitational acceleration  $-g$ . Therefore, the velocity of the spacecraft's main body has to be minimized at the time of additional mass separation at the end of Phase 3 to minimize spacecraft rebound. In this section, we derive the optimum design parameter that minimizes the spacecraft velocity at the end of Phase 3. Here, the viscosity term decreases the system energy and suppresses the rebound. Therefore, this section assumes ideal but severe condition:  $c_f = 0$ .

#### Phase 1: Before spring release

The spacecraft body freely falls vertically from initial altitude  $h_0$  with the initial velocity 0. Here,  $l$  is the natural length of the spring connecting the spacecraft body and additional mass, and  $a$  is the compression amount of the spring. Multiple MEID mechanisms can be expressed by selecting of the sign of  $a$ : positive for the proposed mechanism, negative for the G-MEID-A mechanism, and 0 for the U-MEID mechanism. Solving the equation of motion of Phase 1 with these initial conditions, the displacement and velocity of the spacecraft body and additional mass are expressed as follows:

$$\begin{aligned} x_1(t) &= h_0 - \frac{1}{2}gt^2, \\ x_2(t) &= h_0 + l - a - \frac{1}{2}gt^2, \\ v_1(t) &= -gt, \\ v_2(t) &= -gt. \end{aligned} \quad (5)$$

#### Phase 2: From spring release to landing

The motion of Phase 2 is theoretically analyzed as a vibration free two degrees of freedom undamped system. The

equation of motion in Eq. (2) is rearranged as Eq. (7) using Eqs. (6) and the initial time  $t_0$  in Phase 2:

$$\begin{aligned}\omega_2 &= \sqrt{\frac{k}{m_2}}, \\ \omega_f &= \sqrt{\frac{k_f}{m_1}}, \\ \rho &= m_2/m_1,\end{aligned}\tag{6}$$

$$(1 + \rho)\omega_2^2 = \hat{\omega}_2^2,$$

$$\begin{bmatrix} 1 & 0 \\ 0 & 1 \end{bmatrix} \begin{bmatrix} \ddot{x}_1(t) \\ \ddot{x}_2(t) \end{bmatrix} + \begin{bmatrix} \rho\omega_2^2 & -\rho\omega_2^2 \\ -\omega_2^2 & \omega_2^2 \end{bmatrix} \begin{bmatrix} x_1(t) \\ x_2(t) \end{bmatrix} = \begin{bmatrix} -g - \rho\omega_2^2 l \\ -g + \omega_2^2 l \end{bmatrix}.\tag{7}$$

Equation (7) can be solved with the constants  $p_1, p_2, p_3$  and  $p_4$  as follows:

$$\begin{aligned}x_1(t) &= p_1 \cos \hat{\omega}_2 t + p_2 \sin \hat{\omega}_2 t + p_3 t + p_4 - \frac{g}{2} t^2, \\ x_2(t) &= -\frac{p_1}{\rho} \cos \hat{\omega}_2 t - \frac{p_2}{\rho} \sin \hat{\omega}_2 t + p_3 t + p_4 + l - \frac{g}{2} t^2, \\ v_1(t) &= -\hat{\omega}_2 p_1 \sin \hat{\omega}_2 t + \hat{\omega}_2 p_2 \cos \hat{\omega}_2 t + p_3 - gt, \\ v_2(t) &= \frac{p_1 \hat{\omega}_2}{\rho} \sin \hat{\omega}_2 t - \frac{p_2 \hat{\omega}_2}{\rho} \cos \hat{\omega}_2 t + p_3 - gt.\end{aligned}\tag{8}$$

The initial condition of Phase 2 can be derived utilizing Eq. (1) and the spring release time  $t_0$ . Equations (8) present the following solutions by utilizing the initial condition:

$$\begin{aligned}x_1(t) &= \frac{\rho a}{1 + \rho} \cos \hat{\omega}_2 t - gt_0 t + h_0 - \frac{1}{2} g t_0^2 - \frac{\rho a}{1 + \rho} - \frac{g}{2} t^2, \\ x_2(t) &= -\frac{a}{1 + \rho} \cos \hat{\omega}_2 t - gt_0 t + h_0 - \frac{1}{2} g t_0^2 - \frac{\rho a}{1 + \rho} + l - \frac{g}{2} t^2, \\ v_1(t) &= -\frac{\rho \hat{\omega}_2 a}{1 + \rho} \sin \hat{\omega}_2 t - gt_0 - gt, \\ v_2(t) &= \frac{\hat{\omega}_2 a}{1 + \rho} \sin \hat{\omega}_2 t - gt_0 - gt.\end{aligned}\tag{9}$$

Phase 3: From landing to additional mass separation

The equation of motion in Eq. (3) can be rearranged using Eqs. (6) and the beginning time of Phase 3,  $t_1$ :

$$\begin{bmatrix} 1 & 0 \\ 0 & 1 \end{bmatrix} \begin{bmatrix} \ddot{x}_1(t) \\ \ddot{x}_2(t) \end{bmatrix} + \begin{bmatrix} \rho\omega_2^2 + \omega_f^2 & -\rho\omega_2^2 \\ -\omega_2^2 & \omega_2^2 \end{bmatrix} \begin{bmatrix} x_1(t) \\ x_2(t) \end{bmatrix} = \begin{bmatrix} -g - \rho\omega_2^2 l \\ -g + \omega_2^2 l \end{bmatrix}.\tag{10}$$

Equation (10) can be solved using the constant parameters,  $A_{1a}$ ,  $A_{1b}$ ,  $B_{1a}$ , and  $B_{1b}$ :

$$\begin{aligned}
x_1(t) &= A_{1a} \sin \omega_a t + B_{1a} \cos \omega_a t + A_{1b} \sin \omega_b t + B_{1b} \cos \omega_b t - \frac{(1+\rho)g}{\omega_f^2}, \\
x_2(t) &= A_{1a} \frac{\omega_2^2}{\omega_2^2 - \omega_a^2} \sin \omega_a t + B_{1a} \frac{\omega_2^2}{\omega_2^2 - \omega_a^2} \cos \omega_a t + A_{1b} \frac{\omega_2^2}{\omega_2^2 - \omega_b^2} \sin \omega_b t \\
&\quad + B_{1b} \frac{\omega_2^2}{\omega_2^2 - \omega_b^2} \cos \omega_b t - \frac{(1+\rho)g}{\omega_f^2} - \frac{g}{\omega_2^2} + l, \\
v_1(t) &= A_{1a} \omega_a \cos \omega_a t - B_{1a} \omega_a \sin \omega_a t + A_{1b} \omega_b \cos \omega_b t - B_{1b} \omega_b \sin \omega_b t, \\
v_2(t) &= A_{1a} \frac{\omega_2^2 \omega_a}{\omega_2^2 - \omega_a^2} \cos \omega_a t - B_{1a} \frac{\omega_2^2 \omega_a}{\omega_2^2 - \omega_a^2} \sin \omega_a t + A_{1b} \frac{\omega_2^2 \omega_b}{\omega_2^2 - \omega_b^2} \cos \omega_b t \\
&\quad - B_{1b} \frac{\omega_2^2 \omega_b}{\omega_2^2 - \omega_b^2} \sin \omega_b t,
\end{aligned} \tag{11}$$

$\omega_a$  and  $\omega_b$  are the positive values and  $\omega_a^2$  and  $\omega_b^2$  are set as the solutions of  $p^2$ , as shown in ascending order, respectively:

$$\omega_a^2 = \frac{1}{2} \{ (1+\rho)\omega_2^2 + \omega_f^2 \} - \sqrt{(\omega_2^2 + \rho\omega_2^2 + \omega_f^2)^2 - 4\omega_2^2\omega_f^2}, \tag{12}$$

$$\omega_b^2 = \frac{1}{2} \{ (1+\rho)\omega_2^2 + \omega_f^2 \} + \sqrt{(\omega_2^2 + \rho\omega_2^2 + \omega_f^2)^2 - 4\omega_2^2\omega_f^2}. \tag{13}$$

The initial condition of Phase 3 must be the same as the condition when Eqs. (9) in Phase 2 satisfy  $x_1 = 0$ . Here, the time when Phase 2 satisfies  $x_1 = 0$  is set to  $t_1$  in Eqs. (9). The main body displacement and velocity are set to  $X_1$  and  $V_1$ , and those of the additional mass are set to  $X_2$ , and  $V_2$ , respectively. The displacement and velocity condition are set to the initial condition ( $\tau = t - t_1 = 0$ ) of Phase 3. The following constraints are derived:

$$\begin{aligned}
x_1(0) &= B_{1a} + B_{1b} - \frac{(1+\rho)g}{\omega_f^2} = 0, \\
x_2(0) &= B_{1a} \frac{\omega_2^2}{\omega_2^2 - \omega_a^2} + B_{1b} \frac{\omega_2^2}{\omega_2^2 - \omega_b^2} - \frac{(1+\rho)g}{\omega_f^2} - \frac{g}{\omega_2^2} + l = X_2, \\
v_1(0) &= A_{1a} \omega_a + A_{1b} \omega_b = V_1, \\
v_2(0) &= A_{1a} \frac{\omega_2^2 \omega_a}{\omega_2^2 - \omega_a^2} + A_{1b} \frac{\omega_2^2 \omega_b}{\omega_2^2 - \omega_b^2} = V_2.
\end{aligned} \tag{14}$$

These relationships result in the following conditions.

$$\begin{bmatrix} B_{1a} \\ B_{1b} \end{bmatrix} = \frac{(\omega_2^2 - \omega_b^2)(\omega_2^2 - \omega_a^2)}{(\omega_b^2 - \omega_a^2)\omega_2^2} \begin{bmatrix} \frac{g(1+\rho)\omega_b^2}{\omega_f^2(\omega_2^2 - \omega_b^2)} - X_2 - \frac{g}{\omega_2^2} + l \\ -\frac{g(1+\rho)\omega_a^2}{\omega_f^2(\omega_2^2 - \omega_a^2)} + X_2 + \frac{g}{\omega_2^2} - l \end{bmatrix}, \quad (15)$$

$$\begin{bmatrix} A_{1a} \\ A_{1b} \end{bmatrix} = \frac{(\omega_2^2 - \omega_b^2)(\omega_2^2 - \omega_a^2)}{(\omega_b^2 - \omega_a^2)\omega_2^2} \begin{bmatrix} \frac{1}{\omega_a} \left( \frac{\omega_2^2}{\omega_2^2 - \omega_b^2} V_1 - V_2 \right) \\ \frac{1}{\omega_b} \left( -\frac{\omega_2^2}{\omega_2^2 - \omega_a^2} V_1 + V_2 \right) \end{bmatrix}. \quad (16)$$

The design parameter relationship of Phase 3 can be obtained by assigning these constants to the equation. The energy suppression performance can be maximized when the spacecraft velocity is minimized at the end of Phase 3, by optimizing the additional mass separation time. Here, the spring release time  $t_0$  is one of the important design parameters and can be defined to minimize the spacecraft body speed  $v_1$  of Phase 3 at  $x_1(t) = 0$ . The unknown variables (i.e.,  $V_1$ ,  $X_2$ , and  $V_2$ ) are obtained from the known variables: initial spring compression amount,  $a$ ; main body mass,  $m_1$ ; additional mass,  $m_2$ ; spring constant,  $k$ ; and ground stiffness,  $k_f$ . Therefore, the optimum spring release time can be obtained when all the above variables are defined. One of the potential methods to design these system parameters is performing parameter surveys to maximize rebound suppression by utilizing this section's discussion results together with a Monte–Carlo simulation. The parameters' range can be limited from the system or other constraints. For example, the values of  $m_1$  and  $m_2$  and their ratio can be selected based on system requirements. The structural design requirements constrain the range of  $a$  and  $k$ , for example, the mechanical stiffness has limitations from the environmental condition or structural design.  $k_f$  can be selected from the target body's landing position. However, it has to be confirmed that selected design parameters have the robustness for the  $k_f$  variation limited by the target body's assumptions.

#### IV. Numerical simulations for lunar landing problems

This section involves the numerical simulation study of the proposed mechanism. The characteristics and effectiveness of the proposed method were mainly evaluated by comparing with the G-MEID-A mechanism, which achieves the best rebound suppression performance among the previous studies [17]. First, a case study analysis of the proposed and G-MEID-A mechanisms was performed to confirm the energy and momentum exchange sequence, and the rebound suppression performance. Additional simulations and discussions were then performed to evaluate the robustness against various parameter uncertainties. The robustness analysis was applied to the design parameter variation and target point uncertainties. The numerical simulation results also showed the trend of the design parameter optimization.

The numerical simulation is performed by solving the differential equation derived from the dynamical model constructed in Section III with a fourth-order Runge–Kutta method. All numerical simulations sampling periods were

set as 0.1 ms. The lunar surface landing problems were set as the simulation conditions because of many on-site observation or experiment data, which provide realistic numerical conditions; thus the results can be easily compared to those obtained from an on-ground experiment utilizing previous studies [42]. The maximum rebound amount was used as an evaluation index, as performed in the previous section. The numerical simulation parameters were set, as shown in Table 1, by considering the most challenging landing point whose attenuation parameter assisted rebound [43]. The initial condition also came from the previous study in Ref. [10]. Viscous damping reduced the system energy and helped rebound suppression. Therefore, the smallest viscous damping value was chosen from the reference for the numerical simulation. The optimizable design parameters of the proposed mechanism consisted of the spring restrained release time ( $t_1$ ), the spring constant ( $k$ ), and the additional mass  $m_2$ . Here, the  $m_2$  value was set to 5 kg, nearly 1/10 of the mass ratio of the main body and additional mass. The rebound suppression capability becomes larger as it is proportional to this value because of its momentum exchange effect; however, a smaller mass is desirable for feasibility because of the presence of severe mass constraints. This value is more challenging compared with the previous MEID studies for these applications.

**Table 1 Simulation parameters**

<i>Parameter</i>	<i>Symbol</i>	<i>Value</i>	<i>Unit</i>
<i>Body mass</i>	$m_1$	50.0	kg
<i>Additional damper mass</i>	$m_2$	5.0	kg
<i>Spring natural length</i>	$l$	0.50	m
<i>Spring constant</i>	$k$	2.0	kN/m
<i>Initial compression length</i>	$a$	0.086	m
<i>Initial altitude</i>	$h_0$	3.0	m
<i>Initial velocity</i>	$v_0$	0.0	m/s
<i>Gravitational acceleration</i>	$g$	1.63	m/s <sup>2</sup>
<i>Stiffness between spacecraft and ground</i>	$k_f$	Variable	N/m
<i>Viscous damping between spacecraft and ground</i>	$c_f$	0.2	kN·s/m

#### **A. Comparison of the proposed and G-MEID-A mechanisms through a case study analysis**

This subsection discusses the characteristics and energy balance of the proposed and G-MEID-A mechanisms based on a case study. The parameters were set, as shown in Table 1. The ground stiffness was set to  $k_f = 100$  N/m. The spring separation times were set to 1.718 s for the proposed mechanism and 1.879 s for the G-MEID-A mechanism by the numerical optimization to minimize the maximum rebound amount.

##### *1. Time histories of displacement and acceleration*

Figures 5 and 6 show the time histories of displacement and acceleration. The main bodies were highly accelerated around the landing in both mechanisms. In the proposed mechanism, a downward acceleration was added to the main

body and an upward acceleration to the additional mass at the spring release time. The spring effect was opposite in the G-MEID-A mechanism. The trends and values of the displacement were almost the same in these mechanisms, except for the acceleration histories. These results show that the proposed mechanism can achieve a similar or better rebound suppression performance of the best MEID mechanism compared to the previous studies.

Figure 7 compares the acceleration profile of the spacecraft's main body for the proposed and G-MEID-A mechanisms. The proposed mechanism generates an upward acceleration at landing. This characteristic can mitigate the degradation of rebound suppression performance even if the time of momentum exchange was different from the desired value.

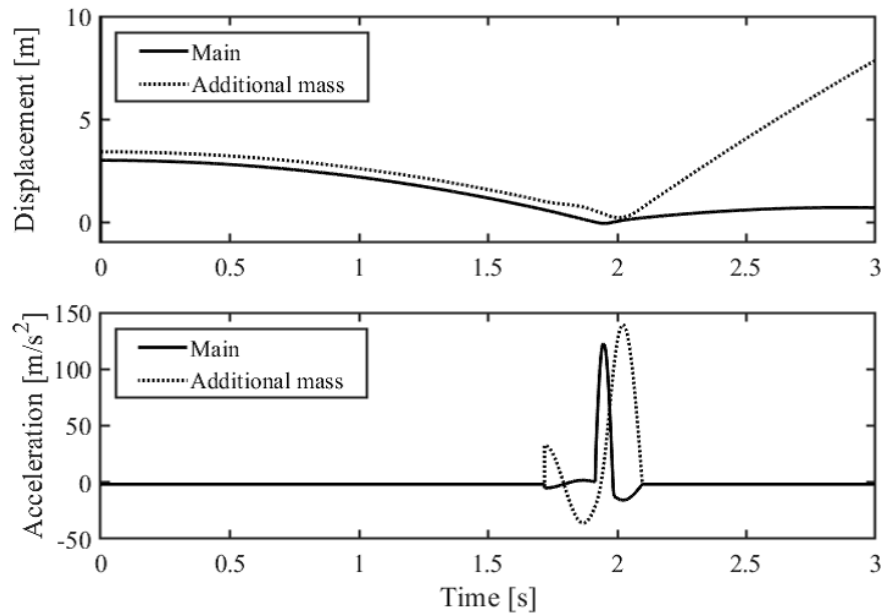


**Fig. 5 Displacement and acceleration histories of the proposed mechanism.**

## 2. Energy budget analysis

This subsection explains the energy budget consisting of the potential energies of the main spacecraft body and additional mass, the kinematic energies of the main spacecraft body and additional mass, and the elastic energies of the spring and ground.

The potential energy equation is

$$Ep_i = m_i g x_i. \quad (i = 1, 2) \quad (17)$$

The kinematic energy equation is

$$Ek_i = \frac{1}{2} m_i v_i^2. \quad (i = 1, 2) \quad (18)$$

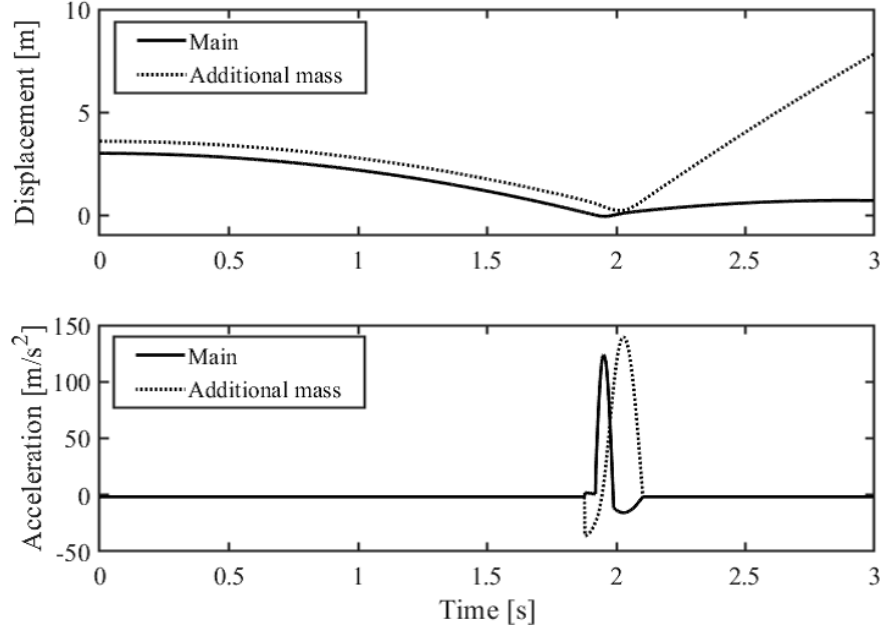


**Fig. 6 Displacement and acceleration histories of the G-MEID-A mechanism.**

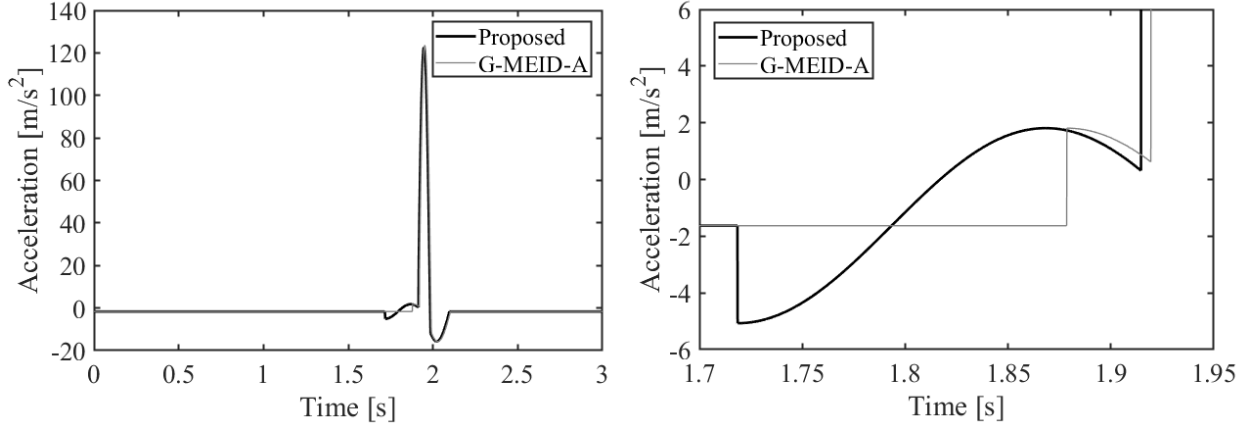


**Fig. 7 (Left) Acceleration profile of the spacecraft main body, with  $k_f = 100$  kN/s, (Right) enlarged.**

The elastic energy equation is

$$Ee_i = \frac{1}{2}k_i\Delta l_i^2, \quad (i = -, f) \quad (19)$$

where,  $\Delta l$  is the displacement of each spring.

Figures 8 and 9 show the time histories of the energies. The upper figures show the kinematic and spring energies. The middle figures show the potential energies. The lower figures summarize the total energy of each component and the whole system. Figures 10 show the energy rate histories when the total system energy of the initial condition

was set to 100%. The upper figures summarize the kinetic and spring energies and the lower figures summarize the potential energies. The total system energy decreased because of energy dissipation by ground viscosity while the spacecraft displacement had negative values.

The comparison of these figures clarifies the differences between the characteristics of different mechanisms. In the proposed mechanism, the spring separation results in energy exchanges between the additional mass and the spacecraft main body. Then, the energy is exchanged between the additional mass as well as spring elastic energy and the spacecraft's main body. The elastic energy of the spring is lost when the spring reaches its natural length. The acceleration of the spacecraft's main body and the additional mass become the gravitational acceleration at that time. Then, the spacecraft's main body energy is exchanged with the additional mass and spring elastic energy. The spring's elastic energy is similar to that of the initial condition, and the spacecraft lands on the ground. At that time, an upward acceleration is imparted to the spacecraft's main body, while a downward one is imparted to the additional mass. After landing, the spacecraft kinematic energy and spring elastic energy are exchanged with the additional mass's kinematic energy and the ground elastic energy while the spacecraft's main body sinks to the ground. The spacecraft main body obtains the kinetic energy by the ground response. At the same time, a part of the kinetic energy of the spacecraft's main body is lost by the viscous ground. The additional mass's kinetic energy becomes the maximum value when the body's acceleration becomes maximum and the additional mass kinetic energy and ground elastic energy are exchanged with the spring elastic energy and kinetic energy of the body. The spacecraft main body is launched after the spring's elastic energy reaches maximum, and the maximum downward acceleration is imparted to the main body. The elastic energy of the spring becomes minimum when the kinetic energy of the additional mass reaches maximum. At that time, the spacecraft energy is reduced by the additional mass injection.

The G-MEID-A mechanism showed almost the same characteristics as the proposed mechanism. However, some differences were found in the energy exchange sequences from the spring separation to the landing phase. In the proposed mechanism, the sum of the kinematic and potential energies of the main spacecraft body increase by spring release. The energy of the additional mass became smaller at the same time. In the G-MEID-A mechanism, the spacecraft's energy was constant, and the additional mass's energy increased after spring release. The energy exchange duration was shorter than that in the proposed method. Additionally, the G-MEID-A mechanism had a little more energy at the beginning of the free fall owing to the potential energy difference associated with the initial spring condition. These differences make the proposed mechanism advantageous to reach maximum rebound dissipation performance.

## **B. Design parameter optimization for landing on a well-known ground without uncertainties**

Design parameter flexibility is one of the important aspects of mechanism evaluation. Therefore, design parameter optimization is numerically performed in this subsection. The spring constant ( $k$ ) and spring release time ( $t_1$ ) were simultaneously optimized. The optimization was performed both for the proposed and G-MEID-A mechanisms to



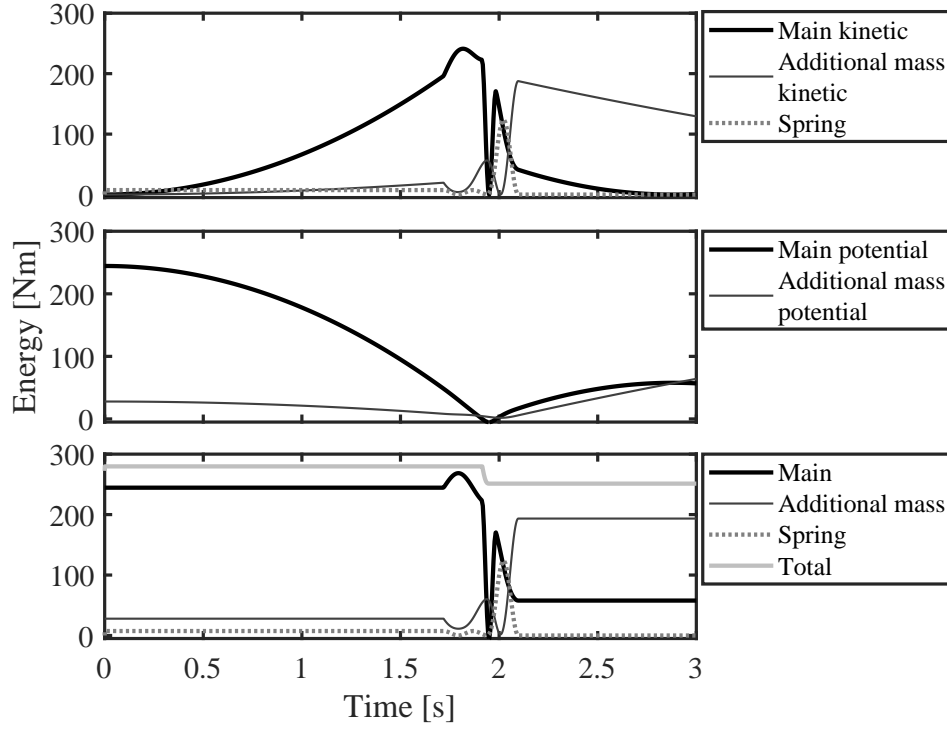


**Fig. 8 Time history of energy of the proposed mechanism.**

compare their characteristics. The same compression amount,  $a$ , was selected for the G-MEID-A mechanism, by only changing its sign. Assuming that the ground rigidity was 20 kN/m and 200 kN/m among the parameters shown in Table 1, the variable parameters were set as the spring stiffness and spring release time. The parameter optimization was performed under these constraints.

Figures 11 and 12 show the relationship between the spring release time, spring stiffness, and maximum rebound amount of the proposed and G-MEID-A mechanisms. The horizontal axis represents the difference between the spring release time and the spacecraft main body's ground landing time. The vertical axis represents the rigidity of the spring connecting the spacecraft body and additional mass. The rebound suppression effect of the main body was large in the portion indicated by black and smaller in that indicated by white. The spring release time was varied every 0.01 s within the range  $\pm 0.2$  s from 1.9186 s, the landing time of the spacecraft without the MEID system. The spring stiffness was varied from 100 N/m to 20 kN/m in increments of 100 N/m.

The proposed mechanism results showed that releasing the spring before landing is more advantageous, regardless of the ground rigidity. The spring release time for the G-MEID-A mechanism must be close to the main body's landing time. If the separation is delayed, the rebound suppression is reduced, and its effect varies depending on the ground stiffness parameters. The rebound suppression capability of the proposed mechanism also changed with

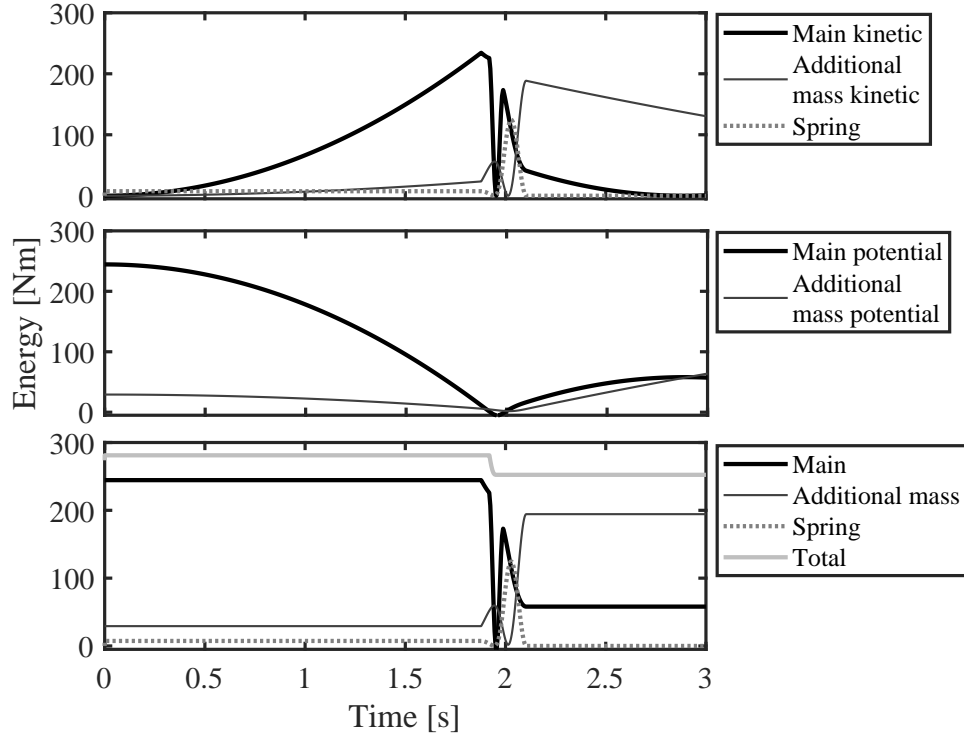


**Fig. 9** Time history of energy of the G-MEID-A mechanism.

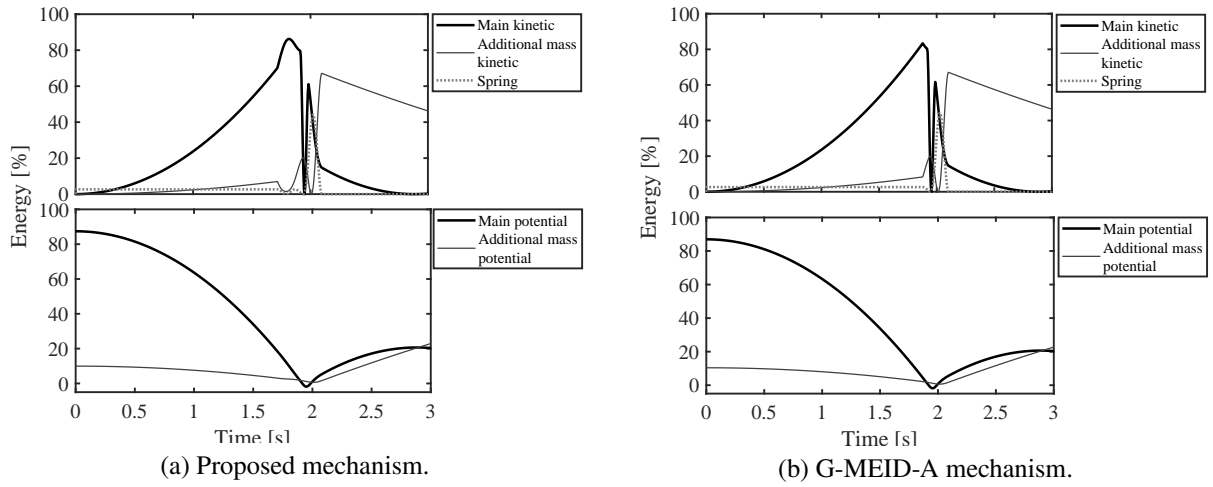


**Fig. 10** Time history of energy rate.

ground stiffness. However, the variation range depending on the ground stiffness was smaller compared with that in the G-MEID-A mechanism. This was also caused by the difference in the energy exchange sequence and duration.

In addition, these simulation results indicate the trend of the design parameter optimization. Both mechanisms tended to suppress the maximum rebound amount of the spacecraft main body when we chose a low-rigidity spring

for a low-rigidity ground and a high-rigidity spring for a high-rigidity ground. In these mechanisms, the rebound suppression was achieved by the exchange of the elastic energy for the impact energy at the time of landing and the momentum exchange between the main body and the additional mass by the additional mass ejection after landing. The impact energy and additional mass's injection force were small when the ground rigidity was high. Therefore, a low-rigidity spring was advantageous here. When the ground had high rigidity, the impact energy was large, and the momentum had to be exchanged between the main body and additional mass. Therefore, a high-rigidity spring was advantageous here.

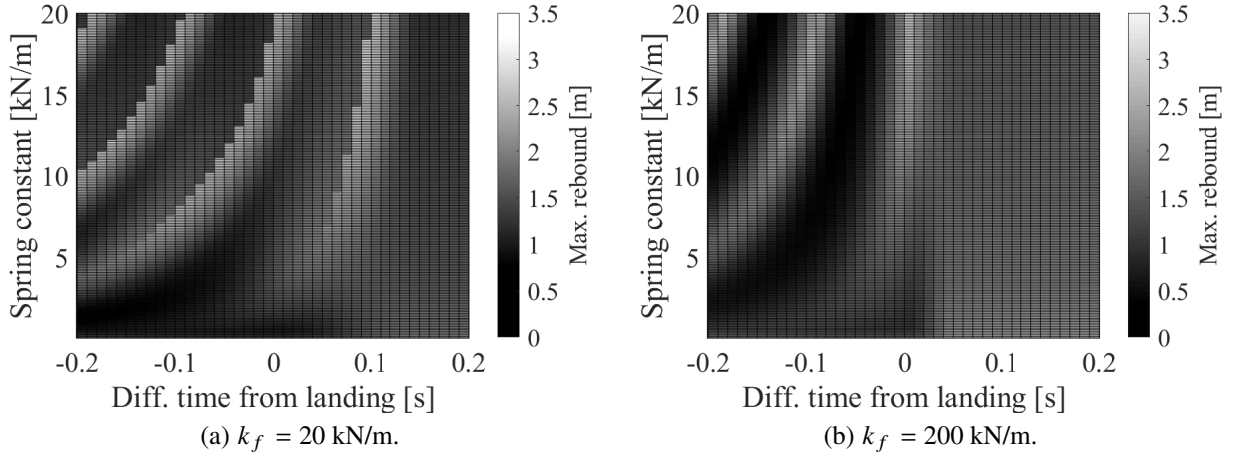


**Fig. 11 Relationships among the separation time of the spring, spring constant, and maximum rebound amount of the spacecraft for the proposed mechanism.**

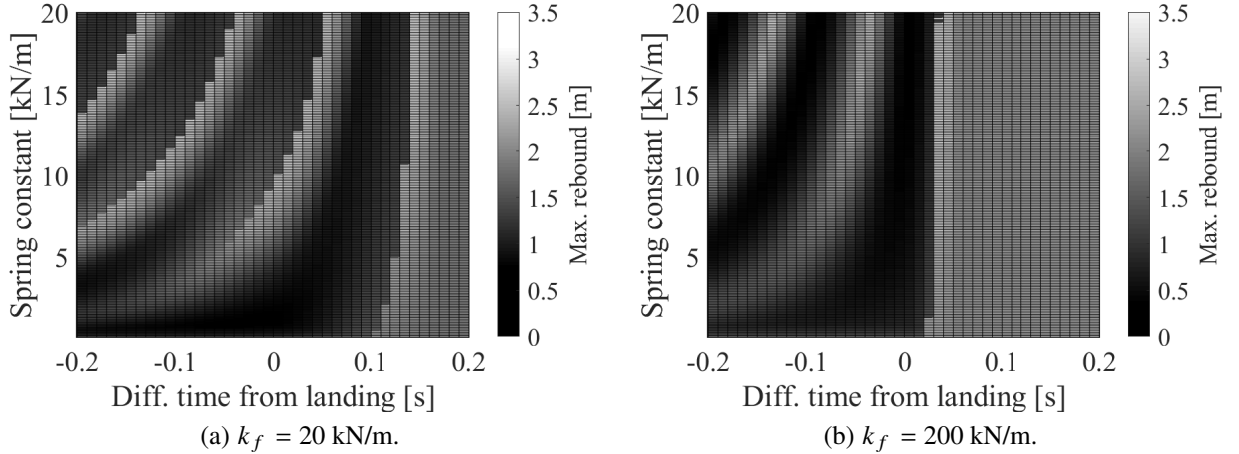


**Fig. 12 Relationships among the separation time of the spring, spring constant, and maximum rebound amount of the spacecraft for the G-MEID-A mechanism.**

### C. Evaluation of robustness against ground stiffness variation

As discussed in the introduction, robustness against ground parameter uncertainties is also an important aspect. In this section, a spacecraft with the parameters listed in Table 1 was used in the numerical simulation. The simulation conditions were set to the optimized parameters described in the previous section. The ground rigidity of the landing site was assumed to be 20 kN/m, and an optimum spring release time of 1.786 s was adopted. Under these conditions, we investigated the influence of varying ground rigidity on the rebound suppression effect.

Figure 13 shows the relationship between the stiffness variation of the landing site and maximum rebound amount of the main spacecraft body, whose spring release time was optimized for the rebound suppression of the assumed ground condition. The simulations were performed on the proposed mechanism, as well as G-MEID-A, and U-MEID mechanisms. Here, the landing site stiffness was varied from 10 kN/m to 400 kN/m in increments of 100 N/m.

The difference in the landing site stiffness degraded the rebound suppression performance in every mechanism. The performance degradation was smaller in the proposed mechanism compared with that in the G-MEID-A mechanism results when the stiffness was larger than the expected value. The stiffness difference caused landing duration differences. It also caused energy exchange differences in the ground, spring, additional mass, and spacecraft's main body. This trend agreed with the parameter optimization results shown in the previous subsection IV B. The energy exchange sequence and duration were different in these mechanisms. The separation time delay had a more prominent effect in G-MEID-A than in the proposed mechanism because the energy exchange duration was shorter in the G-MEID-A mechanism. The U-MEID mechanism did not restrain the spring; hence it had robustness against the ground stiffness variations. However, the rebound suppression effect itself was smaller than the others. The simulation results demonstrate the advantage of the proposed mechanism for achieving robustness against ground stiffness variation.

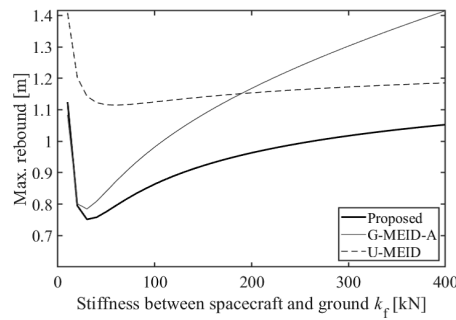


**Fig. 13 Relationships between the ground stiffness and the maximum rebound amount of spacecraft.**

### D. Evaluation of robustness against initial altitude variation

Figure 14 shows the relationship between the initial altitude variation and maximum rebound amount of the main spacecraft body whose spring release time is optimized to be best for rebound suppression for Table 1 parameters

and  $k_f = 20$  kN/m. The simulations were performed on the proposed mechanism and G-MEID-A, and U-MEID mechanisms. Here, the initial altitude of the free fall varied from 2.0 to 4.0 m in increments of 0.02 m.

The optimized altitude of 3.0 m becomes the border of the trend for rebound suppression. If the initial altitude is larger than the optimized altitude, both the proposed and G-MEID-A mechanisms exhibit the same trend for rebound suppression performance. The spring release occurs earlier than the optimized time for the free-fall condition if the initial altitude is higher than 3.0 m. If the initial altitude is lower than 3.0 m, the spring release delays the optimized timing for each free-fall condition. If the landing occurs before the spring release, G-MEID-A and U-MEID mechanisms show the same tendencies, and only the proposed mechanism differ due to the difference in spring energy. Around the optimized altitude, the spring length condition and landing time affect each other, and a complex response can be seen. However, the compressed spring energy better mitigates rebound suppression, and the proposed mechanism is superior to other mechanisms.

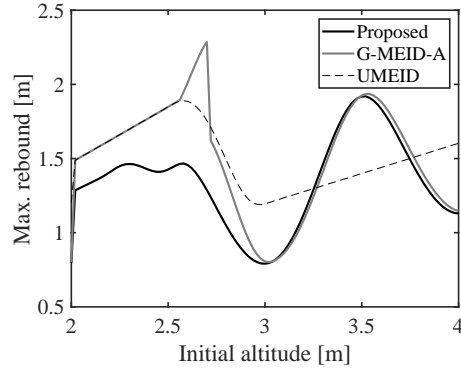


**Fig. 14 Relationship between initial altitude variations and maximum rebound amount of spacecraft.**

### E. Summary of numerical simulations

This section summarizes the characteristics of the proposed mechanism and its robustness to parameter variations through numerical simulations. The previous section's discussion was also confirmed through the numerical simulation. The simulation results showed that the extension of the energy exchange duration improves the robustness. This is caused by simultaneously inheriting the characteristics of both mechanical energy and momentum exchange of the system. This effect mitigated the severe separation time requirement while maintaining the rebound suppression effect of the previous MEID mechanism. However, the main body was highly accelerated around the landing similar to that in the previous MEID mechanism.

The additional numerical simulation results demonstrate the design parameter flexibility of the proposed mechanism in comparison with the previous MEID mechanism results. The proposed method's characteristics, design parameter constraints, or separation time requirement, showed that the rebound suppression capability is less decreased compared

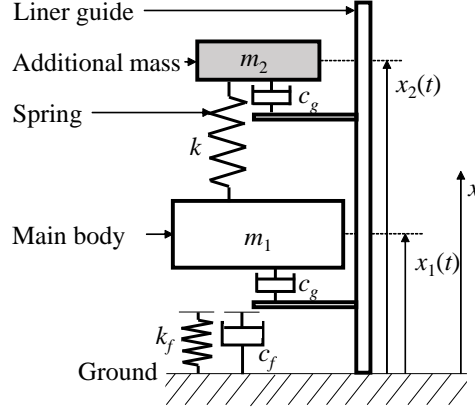


**Fig. 15 Experimental system model.**

with that of the G-MEID-A mechanism. The robustness to the uncertainties was confirmed through numerical simulations with possible variations in the spring separation time, spring constant, and ground stiffness. These parameter variations can be connected to realistic problems. For example, the initial altitude variations can be considered as the separation time variance. The initial altitude variation causes landing time errors. The spring is released earlier than optimized time when the free fall starts at higher than the intended altitude.

The optimization results also provided insight into system design. The ground parameter knowledge helped to enlarge the rebound suppression effect. The optimal spring release time was related to the ground stiffness. When the ground stiffness increased, the landing duration decreased, and the optimal spring separation happened earlier. The spring stiffness was also related to the ground stiffness. The optimal spring stiffness increased when the ground stiffness was larger. Thus, it is important to limit the parameter survey area of Monte-Carlo studies in system parameter design. In addition, the proposed mechanism shows the highest robustness against ground stiffness variation compared with U-MEID, and G-MEID-A mechanisms.

## V. Experimental simulations for lunar landing problems

In this section, we present the free fall experiments performed to confirm the previous section's discussions. A spring with a long length and small stiffness as described in the conclusion of the previous section was selected. Additional terms and unknown parameters were incorporated into the previous model: the viscous friction  $f_{cg}$  of the linear motion guide and the mechanical loss  $f_g$  during the spring separation (Fig. 15). Equation 20 expresses the equation of motion after the spring separation. Viscous friction worked in the direction opposite to motion in proportion to speed,  $f_{cg} = -c_g v$ . Mechanical loss worked in a direction opposite to motion with a constant force. These unknown mechanical parameters originated from one-dimensional constraints, and they were determined through the comparison of numerical and experimental simulation results.

$$\begin{bmatrix} m_1 & 0 \\ 0 & m_2 \end{bmatrix} \begin{bmatrix} \ddot{x}_1(t) \\ \ddot{x}_2(t) \end{bmatrix} + \begin{bmatrix} c_f + c_g & 0 \\ 0 & c_g \end{bmatrix} \begin{bmatrix} \dot{x}_1(t) \\ \dot{x}_2(t) \end{bmatrix} + \begin{bmatrix} k + k_f & -k \\ -k & k \end{bmatrix} \begin{bmatrix} x_1(t) \\ x_2(t) \end{bmatrix} = \begin{bmatrix} -m_1 g + f_g - kl \\ -m_2 g + f_g + kl \end{bmatrix} \quad (20)$$

The proposed mechanism, G-MEID-A, and U-MEID mechanisms were selected for the experiments. Five different ground rigidities were selected to evaluate the rebound suppression performance and robustness against the ground parameter variations.

### A. Experimental system

In the experiments, various design parameters were set using a 1/6G similarity rule [42] to construct an experimental system equivalent to the lunar landing problem. Five materials (from MISUMI Corporation [44]) were selected to apply to the grounds and verify the robustness against ground stiffness variation. The stiffness,  $k_f$ , and the viscosity,  $c_f$ , of each ground are experimentally defined as follows:

- SGNB (SponGe sheet of Nitrile ruBber, Asker: C30)  $k_f = 81.94 \text{ kN/m}$ ,  $c_f = 77.57 \text{ N}\cdot\text{s/m}$
- SUTLL (super-low hardness sheets, shore hardness: A15)  $k_f = 93.28 \text{ kN/m}$ ,  $c_f = 65.00 \text{ N}\cdot\text{s/m}$
- AMSET (AMber color rubber ShEeTs of natural rubber, shore hardness: A45)  $k_f = 700.2 \text{ kN/m}$ ,  $c_f = 177.5 \text{ N}\cdot\text{s/m}$
- RBTMF (nitrile rubber sheet, shore hardness: A50)  $k_f = 3657 \text{ kN/m}$ ,  $c_f = 737.5 \text{ N}\cdot\text{s/m}$
- RBNMF (nitrile rubber sheet, shore hardness: A70)  $k_f = 6614 \text{ kN/m}$ ,  $c_f = 1046 \text{ N}\cdot\text{s/m}$

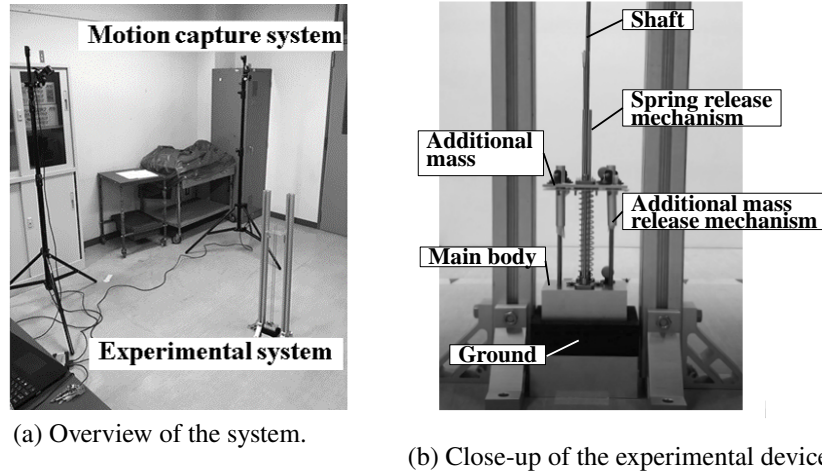
Appendix A presents the details of the ground parameter determination.

Figure 16(a) shows an overview of the experimental and measurement systems. Figure 16(b) shows the details of the experimental device. The experimental system motion was one-dimensionally constrained to apply the numerical simulation model and performed only a free fall experiment. The system consisted of an additional mass, a spring, the main body equipped with a spring release device, and an additional mass release device. Each releasing device consisted of a cylindrical pipe with holes, a screw, and plastic balls. Figure 17 presents the details of the release mechanism. The separation devices had cylindrical pipes. The plastic balls were set into the holes in the pipes and held the connection of the devices by their plate parts. The screws attached at a predetermined altitude extruded the plastic balls to release the connection. The spring was released at a fixed altitude. The release device operation can be derived from the free fall equation, and the spring release can be reproduced using the optimal time.

Table 2 shows the parameters for the experiments. The initial altitude was set to 0.5 m corresponding to a free fall from an altitude of 3m to the lunar surface through the 1/6G similarity rule. The experimental condition was set up using the 1/6 G similarity rule, which defines the ratio of the physical quantities. Here, the ratio of the physical

quantities is assumed the same on the Earth and moon. The displacement was set as  $1/6$ , the velocity remained the same, the acceleration was increased 5 times, and  $1/216$  of the mass was used to emulate the lunar lander's motion under the Earth environment. The experiments were performed using the proposed mechanism, and U-MEID, and G-MEID-A mechanisms. This experiment corresponded to the numerical simulation of the robustness of the ground rigidity in the previous section. The spring release time was set as the optimized parameter of the numerical simulations of the SGNB ground parameter which had the lowest rigidity. The times were set to 0.265 s from the beginning of the free fall in the proposed mechanism and 0.295 s in the G-MEID-A mechanism. The trials for each experimental condition were performed 10 times to ensure their reliability.

Similar to that in the previous section, the maximum rebound amount was the measurement parameter used to evaluate the device performance. The trajectories of the main body and the additional mass were recorded by a motion capture system developed by OptiTrack Japan Co. Ltd. [45]. The measurement data were acquired every 8 ms, and its resolution was approximately 0.02 mm.



**Fig. 16 Experimental system.**

## B. Experimental results

Figure 18 shows the time history displacement results of the proposed and G-MEID-A mechanisms on to the AMSET ground, together with a comparison of the numerical simulation results and primary frame images of the experiments. The spring was kept compressed until the release time in the proposed mechanism. The spring was at the stretched state at the time of landing. The additional mass was also ejected by the energy accumulated in the spring. Moreover, the spring was kept stretched until the release time in the G-MEID-A mechanism. After the landing, the additional mass was injected by the accumulated energy in the spring.

The numerical simulation results also agree with the experimental results, indicating the reliability of the constructed



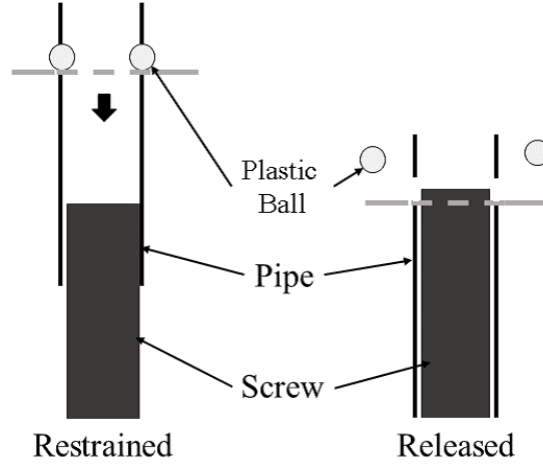


**Fig. 17 Details of the release device.**

**Table 2 Parameters for the experimental simulation**

<i>Parameter</i>	<i>Symbol</i>	<i>Value</i>	<i>Unit</i>
<i>Body mass</i>	$m_1$	0.399	kg
<i>Additional damper mass</i>	$m_2$	0.0576	kg
<i>Spring natural length</i>	$l$	0.10	m
<i>Spring constant</i>	$k$	384	N/m
<i>Initial compression length</i>	$a$	0.02	m
<i>Initial altitude</i>	$h_0$	0.5	m
<i>Initial velocity</i>	$v_0$	0.0	m/s
<i>Gravitational acceleration</i>	$g$	9.807	m/s <sup>2</sup>
<i>Stiffness between spacecraft and ground</i>	$k_f$	Variable	N/m
<i>Viscous damping between spacecraft and ground</i>	$c_f$	Variable	kN·s/m

model. The viscous friction of the linear guide,  $c_g$ , and the mechanical loss,  $f_g$ , were set to 0.09 N·s/m and 8 N, respectively, through the comparison of the experiment and numerical simulation results.

Figures 19 summarize the experimental results of each mechanism and the corresponding numerical simulation results about the averaged maximum rebound amount with the standard deviation for the experimental results. The errors were caused by the measurement errors from the motion capture, spring separation time errors from the mechanical configuration, and energy loss variations during the spring and additional mass separation. The viscous friction of the linear guide ( $c_g$ ) and the mechanical loss ( $f_g$ ) values were the same in numerical simulations in Fig. 18. The lower right figure compares the averaged maximum rebound amount achieved in the experiment.

Table 3 summarizes the experimental results of the energy dissipation rate of each mechanism. The bold values and italic values are the highest and lowest rebound suppression values for each ground condition, respectively. The energy dissipation rate  $\eta$  [%] is defined as:

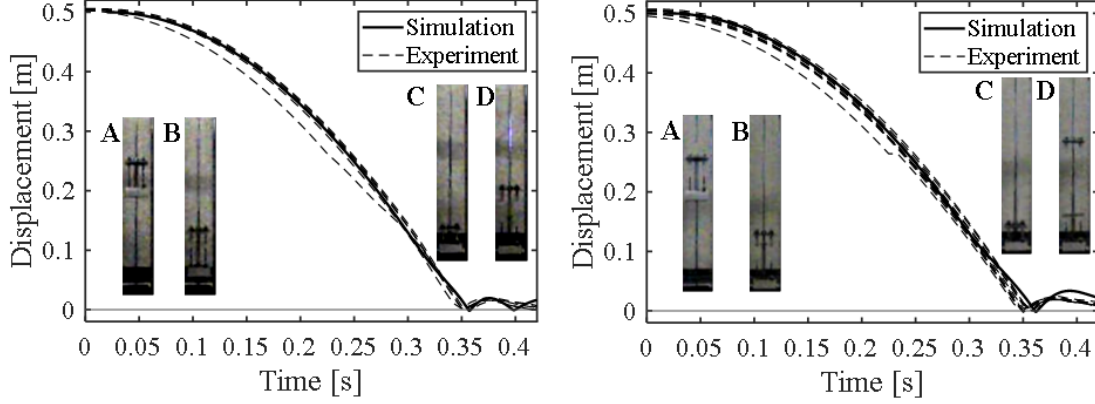


**Fig. 18** Comparison of the experimental and numerical simulation results together with the primary frame images of the experiments; (left) proposed mechanism, (right) G-MEID-A; A) free fall, B) spring release, C) landing, D) additional mass ejection.

$$\eta = \frac{h_0 - h}{h_0} \times 100, \quad (21)$$

where  $h_0$  is the initial altitude, and  $h$  is the maximum rebound amount.

The experimental results showed the advantages of the proposed mechanism compared to the U-MEID mechanism in rebound suppression performance for all ground conditions. The advantage in rebound suppression capability of the proposed mechanism to G-MEID-A mechanism increases, as the ground rigidity increases. The results showed the proposed mechanism's high rebound suppression capability, and its robustness against parameter variations, such as the rigidity and viscosity of the ground, compared to the G-MEID-A mechanism. The experimental results' tendencies agree with the previous sections' discussions, and support their validity. Here, the discussions only consider the ground that can be modeled as a combination of the spring and damper, as shown in the previous section. For different characteristics ground models, a case study is discussed in Appendix B.

**Table 3** Experimental results of energy dissipation rate for each mechanism, %

<i>Mechanism</i>	<i>SGNB</i>	<i>SUTLL</i>	<i>AMSET</i>	<i>RBTMF</i>	<i>RBNMF</i>
<i>Proposed</i>	<b>91.1</b>	<b>89.7</b>	<b>85.8</b>	<b>81.9</b>	<b>82.8</b>
<i>G-MEID-A</i>	89.2	88.3	83.3	74.3	70.1
<i>U-MEID</i>	83.9	81.7	82.7	76.0	71.0

## VI. Case Study: Combined Application to Microgravity Bodies' Landing Problem

The previous sections performed the ground experiment assuming the lunar landing problem and compared it with the numerical simulation results because it has the confirmed relationship between the ground experiment and the real

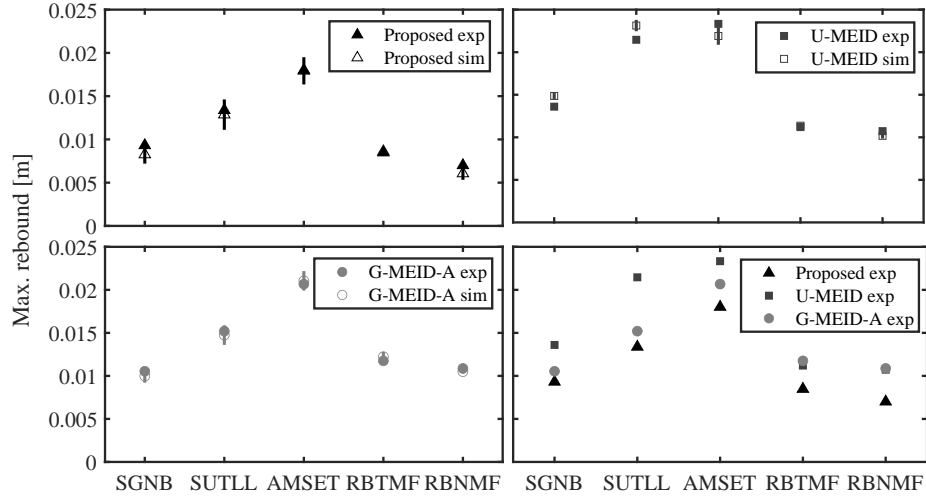


**Fig. 19 Experimental results.**

landing problem. The results showed that the proposed mechanism is effective and robust for delivering high rebound suppression performance despite landing site variations, such as rigidity and viscosity. Some unmodeled aspects to realize the experimental mechanism were also added to the simplified conceptual model, and those parameters were identified by the experimental results. However, as shown in Fig. 7 in Section IV, the capability to mitigate shock acceleration provided by only the proposed mechanism, if it is applied to the lunar landing problem, is not so high.

From these characteristics, additional case studies for the proposed mechanisms are discussed. As explained in Section II, the landing problem of microgravity celestial bodies has a critical rebound suppression requirement, and their landing site parameters demonstrate a wide range of uncertainties. In this case study, the disadvantage of the acceleration mitigation performance was overcome by combining the proposed mechanism with other mechanisms to reduce shock acceleration. During the landing on microgravity celestial bodies, even a tiny residual energy causes rebound, and a single landing mechanism cannot achieve severe energy dissipation requirement.

This section shows the case study results, in which the proposed mechanism dissipates the remaining energy through the metal-plastic deformation of the shock absorber. The effect is verified through the numerical simulations of the case of microgravity exploration probe, future program, called Martian Moons eXploration (MMX), plans to land to Mars' satellite Phobos. The MMX's spacecraft will be launched in 2024. The energy dissipation requirement for the MMX was set as the numerical simulation conditions in this section. Over 99% energy dissipation must be achieved for this mission to decrease the overturning risk [11, 24].

Table 4 shows the numerical simulation conditions. In Ref. [25], the system has 4 landing gears and each mass is 10 kg, and the total system mass is 1700 kg. Therefore, the main body mass is set as 400 kg, and footpad is set as

**Table 4 MMX simulation parameters**

<i>Parameter</i>	<i>Symbol</i>	<i>Value</i>	<i>Unit</i>
<i>Body mass</i>	$m_1$	400	kg
<i>Footpad mass</i>	$m_{ft}$	10	kg
<i>Shock absorber length</i>	$l$	3	m
<i>Initial altitude</i>	$h_0$	10.0	m
<i>Initial velocity</i>	$v_0$	0.0	m/s
<i>Gravitational acceleration</i>	$g$	0.0049	m/s <sup>2</sup>
<i>Stiffness between spacecraft and ground</i>	$k_f$	60	kN/m
<i>Viscous damping between spacecraft and ground</i>	$c_f$	0.2	kN·s/m

10 kg. The gravity was 1/2000 of the Earth, and the initial altitude of the free fall was 10 m. The celestial body surface condition had uncertainties even though it can achieve proximity for the actual landing. Therefore, rock surface, which can easily cause rebound, was assumed as the worst-case scenario for the rebound suppression problems. This value is the same as in the previous section. A reaction force to the shock absorber was assumed to work by the ground stiffness,  $k_f$ , while the leg tip was on the negative side of the ground surface. A footpad was mounted on the tip of the leg.

The material of the shock absorber was assumed to be an open-cell type porous metal made of AlSi10Mg whose Young's modulus was 70 GPa, yield stress was 220 MPa, and porosity was 93%. Ideally, this shock absorber keeps exerting a constant force of 200 N during plastic deformation [46].

The proposed landing mechanism was systematically evaluated. First, the performance of the shock absorbing material itself was confirmed through the numerical simulation. Figure 20 shows the time histories of the spacecraft body, footpad, and leg length displacements. Here, this figure starts from when the footpad reached a 1.5 m altitude. The maximum rebound amount was 0.132 m, and its energy dissipation rate was 98.7%. This value does not satisfy the requirement for the rebound suppression energy for the MMX mission.

Next, numerical simulations were performed for the proposed landing mechanism, which consisted of the shock absorber and proposed MEID mechanism. The energy dissipation performance was improved by combining it with the proposed mechanism. The natural length of the spring was set to 0.5 m. The initial compression amount was set to 0.3 m. The spring stiffness was set to 300 N/m. The additional damper mass was set to 15.0 kg. In Ref. [26], the mass budget table of the Philae system shows its total mass is 97.89 kg and the sum of the landing mechanism is 13.94 kg. Here, the mechanism comprises an active descent system, anchors, and landing gear, whose mass is 15% of the total system. The proposed system mass is 425 kg in total and the landing system mass is 25 kg, which is 6% of the total system mass.

Figure 21 shows the time history of the displacement of the spacecraft body, damper mass, footpad, and leg length. This figure also starts from when the footpad reached a 1.5 m altitude. The maximum rebound amount was 0.085 m,

and its energy dissipation rate was 99.15%. Figure 22 shows the energy dissipation results under the stiffness between spacecraft and ground, other simulation parameters are the same as Fig. 21. This result shows the proposed system has some robustness for the ground parameter variations. These results showed the feasibility of landing with a high energy dissipation requirement such as on microgravity celestial bodies using the proposed landing mechanism. The MEID mechanism achieved the rebound suppression with the additional compression of the shock absorber in addition to the energy and momentum exchange to the additional mass. In combination with the proposed MEID mechanism, a higher energy dissipation can be achieved which cannot be achieved only by using a conventional method, such as the shock absorber.

The numerical case study results present the effectiveness of the proposed concept; however, this work only considers the one-dimensional motion. To apply this concept to real problems, there are many aspects to be discussed, such as three-dimensional motions. For example, the risks for tip-over have to be considered in three-dimensional analysis. Many other sources could deteriorate landing performance, such as errors during landing, mass injection timing, and the effect of the moment, or horizontal acceleration. We have to perform more specific and realistic analysis to apply this system to real problems. Moreover, the effect of energy storage in the lander structure also has to be considered for realistic analysis. We provide a brief discussion on this topic in Appendix C.

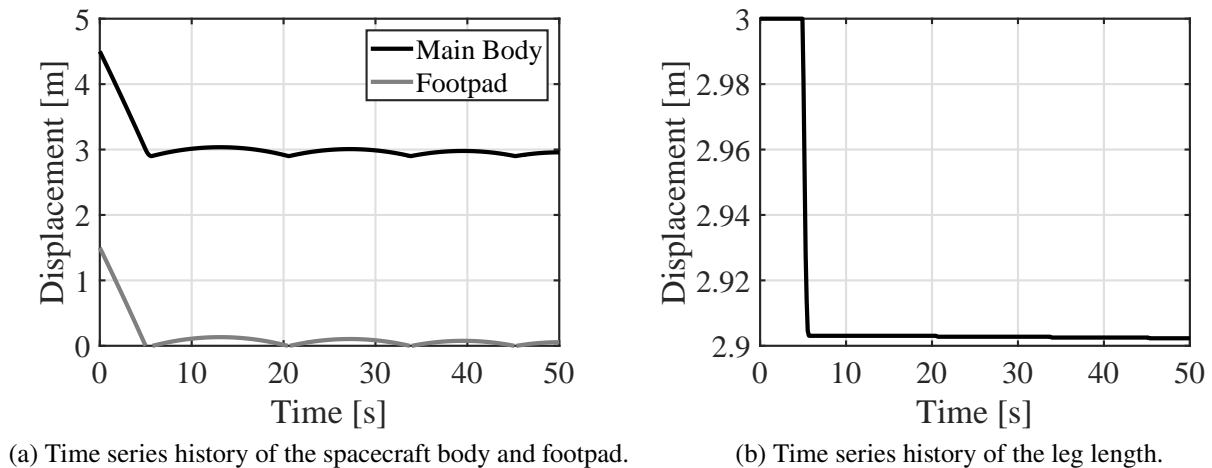
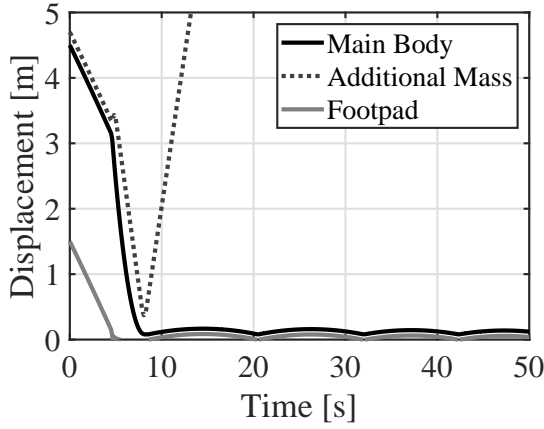


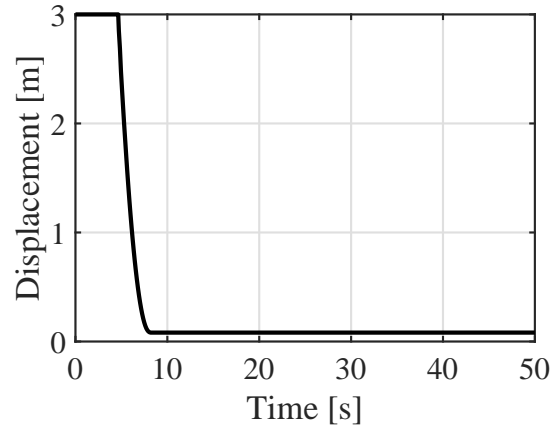
**Fig. 20 Performance of the shock-absorber.**

## VII. Conclusion

This study proposes a robust rebound suppression mechanism by utilizing an additional mass and spring. It simultaneously considers the characteristics of both mechanical energy and momentum exchange. The proposed mechanism can be achieved without complexity and with high rebound suppression capability and robustness despite arbitrary landing site conditions. The system is lightweight and reusable in the ground-verification phase. The design



(a) Time series history of the spacecraft body, the damper mass, and footpad.



(b) Time series history of the leg length.

**Fig. 21 Performance of the shock-absorber and proposed landing mechanism.**

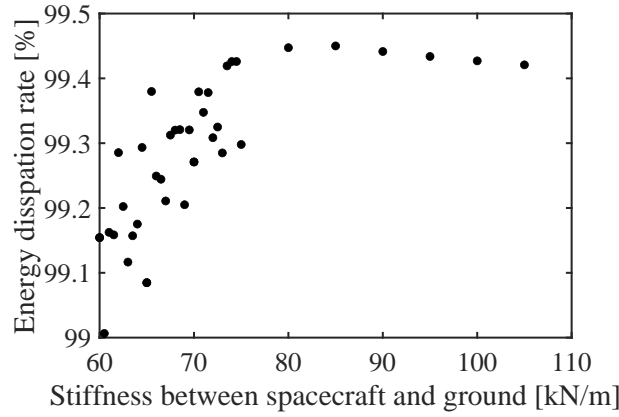


**Fig. 22 Energy dissipation rate under ground stiffness variations.**

characteristics were primarily clarified mainly through numerical discussions. The relationships between the design parameters and their design methods were also discussed with the help of a simplified conceptual model.

Various numerical simulations were performed to verify the effects of possible parameter variations. Especially, robustness against surface property variation was investigated because the surface properties of the landing point are unknown during the design phase of the spacecraft. The results showed the comparable rebound suppression capability and improvement in robustness against unknown surface parameters compared to the mechanism which shows the best rebound suppression capability among the previous momentum exchange impact damper (MEID) series. These results are due to the longer energy exchange duration, and the effect of simultaneously taking into account the characteristics of both the mechanical energy and momentum exchange of the system. Our approach achieves the mitigation of extremely sensitive separation time requirement while maintaining the rebound suppression capability. However, the

main body was highly accelerated around the landing as with the previous mechanism.

The verification of the constructed mechanism was also performed through numerical and experimental simulations for the lunar landing problems, whose correlation between the on-ground experiment and realistic landing conditions is already known from previous studies. The results show the effectiveness of the rebound suppression performance of the proposed mechanism in comparison to other momentum exchange mechanisms.

An additional case study was also performed to show the applicability of the proposed mechanism to microgravity celestial body landings. This proposal was considered to perform the remaining energy dissipations of the other shock absorber. The simulation condition is set up assuming an imaginary microgravity exploration, referring to a project that aims to land on the Martin satellite Phobos in the future. The results showed the potential application opportunities of the proposed system in addition to the single utilization opportunities. However, landing on microgravity celestial bodies has different characteristics from landing on a planet or large moon, and the influence of the non-gravitational effect becomes larger in a real environment. The current discussion focuses only on the rigid lander, its gravity effects, and a more detailed analysis has to be performed to apply this system to a realistic problem.

### A. Ground parameters identification

The ground is considered as a spring-damper model, as shown in Fig. 23. Ground parameters  $k_f$  and  $c_f$  can be obtained using the experimentally identified reflection coefficient  $e_1$ , and ground contact duration  $t_0$ . The experimental mass is set as  $m_1$ .

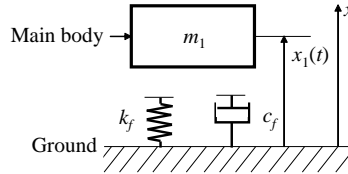


**Fig. 23 Model of the connecting part between the body and ground.**

The equation of motion becomes:

$$m_1 \ddot{x}_1 + c_f \dot{x}_1(t) + k_f x_1(t) = 0. \quad (22)$$

Here, the initial condition at the landing time is set as follows:

$$\begin{aligned} x_1(0) &= 0, \\ \dot{x}_1(0) &= v_0, \end{aligned} \quad (23)$$

where,  $v_0$  is the velocity of the mass prior to landing.

The displacement of the experimental mass can be derived from Eq. (22):

$$x_1(t) = \frac{v_0}{\omega\sqrt{1-\zeta^2}} \exp(-\zeta\omega t) \sin(\omega\sqrt{1-\zeta^2}t), \quad (24)$$

where,

$$\begin{aligned} \omega &= \sqrt{\frac{k_f}{m_1}}, \\ \zeta &= \frac{c_f}{2\sqrt{m_1 k_f}}. \end{aligned} \quad (25)$$

The ground contact duration  $t_0$  is the duration from the landing to the time when the spring returns to the static state:

$$t_0 = \frac{\pi}{\omega\sqrt{1-\zeta^2}}. \quad (26)$$

The reflection coefficient  $e_1$  is the ratio between the velocities before and after contact and can be expressed as:

$$\begin{aligned} e_1 &= -\frac{\dot{x}_1(t_0)}{v_0} \\ &= \exp\left(-\frac{\pi\zeta}{\sqrt{1-\zeta^2}}\right). \end{aligned} \quad (27)$$

Therefore, ground parameters  $k_f$  and  $c_f$  can be derived with the measurable variables, mass  $m_1$ , reflection coefficient  $e_1$ , and ground contact duration  $t_0$  as:

$$\begin{aligned} k_f &= \frac{m_1}{t_0^2} \{(\ln e_1)^2 + \pi^2\}, \\ c_f &= -2m_1 \frac{\ln e_1}{t_0}. \end{aligned} \quad (28)$$

The experiment was performed by the free fall of an aluminum plate with a conductor. A thin aluminum sheet was set on the ground, and the contact duration was measured by the energized duration through the oscilloscope. The sampling period was 0.5 ms. The reflection coefficient was measured by the time series displacement captured by the motion capture system, as explained in Section V.B. The experimental conditions and trial numbers were also similar to those presented in Section V. Table 5 summarizes the results of the experiments and identifications. The standard deviation is shown with a  $\pm$  sign.



**Table 5 Experimental results of landing ground parameters**

Landing ground	$t_0$ [ms]	$e_1$ [-]	$k_f$ [kN/m]	$c_f$ [N·s/m]
SGNB	6.5±0.16	0.466±0.018	81.94±3.80	77.57±4.13
SUTLL	6.0±0.00	0.552±0.007	93.28±1.28	65.00±1.29
AMSET	2.3±0.46	0.548±0.017	700.2±21.4	177.5±30.6
RBTMF	1.0±0.05	0.326±0.015	3657±34.8	737.5±31.0
RBNMF	0.75±0.01	0.307±0.053	6614±232.7	1046±148.7

### B. Case study using another ground model

This study focuses on mechanisms that can provide the robustness against ground surface uncertainties; however, the main discussions consider only the ground, which can be modeled by the spring and damper. Assuming a one-dimensional rebound suppression problem, rebound tends to be easier in the utilized model than with highly dissipative materials such as sand or regolith. This means that the numerical analysis was performed under worst-case scenario. Previous studies have shown that the ground modeling of the sand or regolith is not the same as the ground that of rubber. Therefore, the ground model has to be modified. Equation (29) shows an example model of the force  $F$  developed on the footpad from a soft surface derived from the experience of Surveyor missions [47]:

$$F = p_0 A (1 + cs) + \frac{\rho_1 \rho_1}{\rho_2 - \rho_1} A \dot{s}^2. \quad (29)$$

where,  $p_0$  is the static bearing pressure of the surface ( $3.4 \times 10^4$  N/m<sup>2</sup>),  $A$  is the effective footpad area,  $c$  is the frictional constant ( $3.3$  m<sup>-1</sup>),  $s$  is the depth of penetration,  $\dot{s}$  is the velocity of penetration,  $\rho_1$  is the original density of soil ( $1.2 \times 10^3$  kg/m<sup>3</sup>), and  $\rho_2$  is the density of soil compressed by footpad ( $1.6 \times 10^3$  kg/m<sup>3</sup>). The parameters are defined in Ref. [48].

The numerical simulations were performed with the modified ground model using the same proposed system. Here, the viscous friction of the linear motion guide and mechanical loss were considered 0 to simplify the problem. The effective footpad area was 0.004 m<sup>2</sup> from the dimensions of the main body.

The obtained results were compared with the numerical simulation with SGNB results. Figure 24 shows the effect of delay on separation time. Here, the separation time was 0.265 s which is ideal value for the SGNB ground. Figure 25 shows the time histories of the displacement of the main bodies with the ideal separation time for each ground. In both figures, SGNB shows the results for the spring and damper ground, and regolith shows the results for the modified ground. The experimental results show similar tendencies in rebound suppression performances despite the ground material differences.

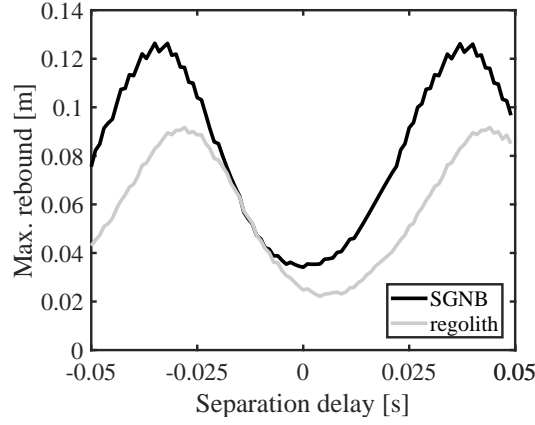


**Fig. 24 Relationships between the separation time delay and the maximum rebound amount of spacecraft.**

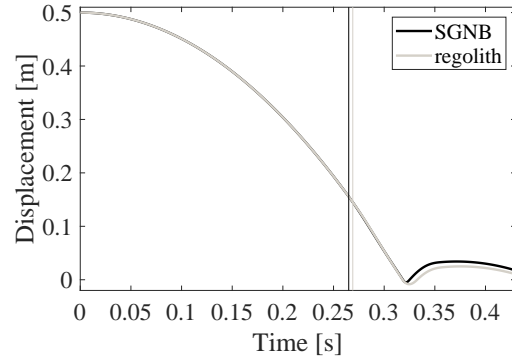


**Fig. 25 Time histories of the displacement of the main bodies with the ideal separation time.**

### C. Effect of energy storage in the lander structure

The experimental system of this study is characterized by high-rigidity; however, the lightweight lander tends to have a flexible structure. In this case, the stiffness of the landing gear or spacecraft structure has to be considered for a more realistic analysis. Therefore, this section performs an additional numerical analysis. Figure 26 shows the modified system model. The stiffness and mass of the landing gear were modeled based on the established model, by dividing the main body model into two components: the main body and landing gear. These two components were combined with the spring element, whose natural length is  $l_g$ , and spring constant is  $k_g$ .

The landing gear, main body, and additional mass are defined as  $m_1$ ,  $m_2$ , and  $m_3$ , respectively. The displacement, velocity, and acceleration of the landing gear, main body, and additional mass are defined as  $x_1$ ,  $x_2$ ,  $x_3$ ,  $\dot{x}_1$ ,  $\dot{x}_2$ ,  $\dot{x}_3$ ,  $\ddot{x}_1$ ,  $\ddot{x}_2$ , and  $\ddot{x}_3$ , respectively. The equation of motion after the spring separation can be expressed as Eq. (30).

$$\begin{bmatrix} m_1 & 0 & 0 \\ 0 & m_2 & 0 \\ 0 & 0 & m_3 \end{bmatrix} \begin{bmatrix} \ddot{x}_1(t) \\ \ddot{x}_2(t) \\ \ddot{x}_3(t) \end{bmatrix} + \begin{bmatrix} c_f & 0 & 0 \\ 0 & 0 & 0 \\ 0 & 0 & 0 \end{bmatrix} \begin{bmatrix} \dot{x}_1(t) \\ \dot{x}_2(t) \\ \dot{x}_3(t) \end{bmatrix} + \begin{bmatrix} k_g + k_f & -k_g & 0 \\ -k_g & k_g + k & -k \\ 0 & -k & k \end{bmatrix} \begin{bmatrix} x_1(t) \\ x_2(t) \\ x_3(t) \end{bmatrix} = \begin{bmatrix} -m_1 g + k l_g \\ -m_2 g - k l_g + k l \\ -m_3 g - k l \end{bmatrix} \quad (30)$$

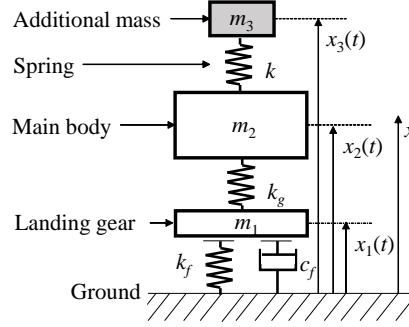


**Fig. 26 Model with the landing gear.**

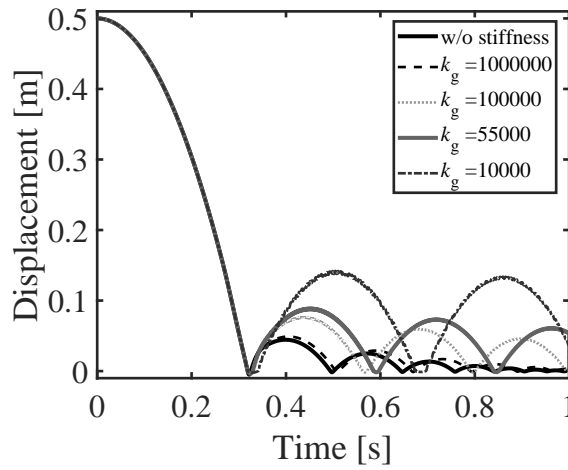


**Fig. 27 Maximum rebound amount under landing gear stiffness variations.**

A case study was conducted using this model. The main parameters were defined as shown in Table 2 by considering the landing problems on the SGNB ground. The spring release time was set as 0.265 s,  $l_g$  was 0.1 m, whereas  $k_g$  was varied. Figure 27 shows the maximum rebound amount under landing gear stiffness variations. The maximum rebound amount increased as the stiffness decreases. When the stiffness increased, the rebound amount was almost the same as that without considering landing gear stiffness. Thus, we have to include the landing gear's stiffness in case of high flexibility. For example, Rosetta lander uses a stiffness of  $5.5 \times 10^4$  N/m [49]. The effects of the landing gear stiffness and its frequency cannot be ignored for realistic considerations.

### Acknowledgments

This work was supported by Japan Society for the Promotion of Science KAKENHI grant number 26249023.

## References

- [1] Ciesla, F., and B. Charnley, S., “The Physics and Chemistry of Nebular Evolution,” *Meteorites and the Early Solar System II*, 2006, pp. 209–230.
- [2] Bhandari, N., “Planetary exploration: Scientific importance and future prospects,” *Current Science*, Vol. 94, No. 2, 2008, pp. 185–200.
- [3] Besse, S., Vallat, C., Barthelemy, M., Coia, D., Costa, M., Marchi, G. D., Fraga, D., Grotheer, E., Heather, D., Lim, T., Martinez, S., Arviset, C., Barbarisi, I., Docasal, R., Macfarlane, A., Rios, C., Saiz, J., and Vallejo, F., “ESA’s Planetary Science Archive: Preserve and present reliable scientific data sets,” *Planetary and Space Science*, Vol. 150, 2018, pp. 131–140. doi:<https://doi.org/10.1016/j.pss.2017.07.013>.
- [4] Kawaguchi, J., Fujiwara, A., and Uesugi, T., “Hayabusa—Its technology and science accomplishment summary and Hayabusa-2,” *Acta Astronautica*, Vol. 62, No. 10, 2008, pp. 639–647. doi:<https://doi.org/10.1016/j.actaastro.2008.01.028>.
- [5] Dunham, D. W., Farquhar, R. W., McAdams, J. V., Holdridge, M., Nelson, R., Whittenburg, K., Antreasian, P., Chesley, S., Helfrich, C., Owen, W. M., Williams, B., Veverka, J., and Harch, A., “Implementation of the First Asteroid Landing,” *Icarus*, Vol. 159, No. 2, 2002, pp. 433–438. doi:<https://doi.org/10.1006/icar.2002.6911>.
- [6] Watanabe, S.-i., Tsuda, Y., Yoshikawa, M., Tanaka, S., Saiki, T., and Nakazawa, S., “Hayabusa2 Mission Overview,” *Space Science Reviews*, Vol. 208, No. 1, 2017, pp. 3–16. doi:[10.1007/s11214-017-0377-1](https://doi.org/10.1007/s11214-017-0377-1).
- [7] Lauretta, D. S., Balram-Knutson, S. S., Beshore, E., Boynton, W. V., Drouet d’Aubigny, C., DellaGiustina, D. N., Enos, H. L., Golish, D. R., Hergenrother, C. W., Howell, E. S., Bennett, C. A., Morton, E. T., Nolan, M. C., Rizk, B., Roper, H. L., Bartels, A. E., Bos, B. J., Dworkin, J. P., Highsmith, D. E., Lorenz, D. A., Lim, L. F., Mink, R., Moreau, M. C., Nuth, J. A., Reuter, D. C., Simon, A. A., Bierhaus, E. B., Bryan, B. H., Ballouz, R., Barnouin, O. S., Binzel, R. P., Bottke, W. F., Hamilton, V. E., Walsh, K. J., Chesley, S. R., Christensen, P. R., Clark, B. E., Connolly, H. C., Crombie, M. K., Daly, M. G., Emery, J. P., McCoy, T. J., McMahon, J. W., Scheeres, D. J., Messenger, S., Nakamura-Messenger, K., Richter, K., and Sandford, S. A., “OSIRIS-REx: Sample Return from Asteroid (101955) Benu,” *Space Science Reviews*, Vol. 212, No. 1, 2017, pp. 925–984. doi:[10.1007/s11214-017-0405-1](https://doi.org/10.1007/s11214-017-0405-1).
- [8] Lauretta, D., “An overview of the OSIRIS-REx asteroid sample return mission,” *43rd Lunar and Planetary Science Conference*, 2012. 43.
- [9] Dreyer, C. B., Abbud-Madrid, A., Atkinson, J., Lampe, A., Markley, T., Williams, H., McDonough, K., Canney, T., and Haines, J., “A new experimental capability for the study of regolith surface physical properties to support science, space exploration, and in situ resource utilization (ISRU),” *Review of Scientific Instruments*, Vol. 89, No. 6, 2018. doi:[10.1063/1.5023112](https://doi.org/10.1063/1.5023112), 064502.

- [10] Shigeto, S., Fujimoto, H., Hori, Y., Otsuki, M., and Hashimoto, T., “Fundamental Research on Reduction of Impact Forces Using Actively Controlled Landing Gear in Lunar/Planetary Landers,” *IEEE Transactions on Industry Applications (in Japanese)*, Vol. 133, No. 3, 2013, pp. 335–341. doi:10.1541/ieejias.133.335.
- [11] Kawakatsu, Y., Kuramoto, K., Ogawa, N., Ikeda, H., Ono, G., Sawada, H., Imada, T., Otsuki, M., Otake, H., Muller, R., Zacny, K., Satoh, Y., Yamada, K., Mary, S., Grebenstein, M., and Yoshikawa, K., “Mission Definition of Martian Moons eXploration (MMX),” *70th International Astronautical Congress 2019, IAC 2019*, 2019.
- [12] Saeki, N., Hara, S., and Otsuki, M., “Two-Dimensional Experimental Investigation of Base-Extension Separation Mechanism with Telescopic Gear,” *Journal of Spacecraft and Rockets*, Vol. 54, No. 1, 2017, pp. 169–190. doi:10.2514/1.A33382.
- [13] Kushida, Y., Watanabe, T., Hara, S., and Otsuki, M., “Dynamics of Lunar/Planetary Exploration Spacecraft Landing Gear Based on Momentum Exchange Principle in Two-Dimensional Motion,” *Aerospace Technology Japan, The Japan Society for Aeronautical and Space Sciences*, Vol. 15, 2016, pp. 43–52. doi:10.2322/astj.15.43.
- [14] Iio, T., Matsuhisa, H., Utsuno, H., Yamada, K., and Sawada, K., “Reduction of landing impact of spacecraft by means of momentum exchange,” *Proceedings of 54th Space Sciences and Technology Conference (in Japanese)*, 2010. JSASS-2010-4111.
- [15] Hara, S., Ito, R., Otsuki, M., Yamada, Y., Kubota, T., Hashimoto, T., Matsuhisa, H., and Yamada, K., “Momentum-Exchange-Impact-Damper-Based Shock Response Control for Planetary Exploration Spacecraft,” *Journal of Guidance, Control, and Dynamics*, Vol. 34, No. 6, 2011, pp. 1828–1838. doi:10.2514/1.53786.
- [16] Hara, S., Watanabe, T., Kushida, Y., Otsuki, M., Yamada, Y., Matsushisa, H., Yamada, K., Hashimoto, T., and Kubota, T., “Study on Landing Response Control of Planetary Exploration Spacecraft Based on Momentum Exchange Principles,” *Transactions of the Japan Society of Mechanical Engineers Series C (in Japanese)*, Vol. 78, No. 792, 2012, pp. 2781–2796. doi:10.1299/kikaic.78.2781.
- [17] Watanabe, T., Hara, S., and Otsuki, M., “Study on landing response control of planetary exploration spacecraft using advanced G-MEID,” *Transactions of the JSME (in Japanese)*, Vol. 81, No. 829, 2015. doi:10.1299/transjsme.14-00006, 14-00006.
- [18] Jurado, E., Martin, T., Canalias, E., Blazquez, A., Garmier, R., Ceolin, T., Gaudon, P., Delmas, C., Biele, J., Ulamec, S., Remeteau, E., Torres, A., Laurent-Varin, J., Dolives, B., Herique, A., Rogez, Y., Kofman, W., Jorda, L., Zakharov, V., Crifo, J.-F., Rodionov, A., Heinisch, P., and Vincent, J.-B., “Rosetta lander Philae: Flight Dynamics analyses for landing site selection and post-landing operations,” *Acta Astronautica*, Vol. 125, 2016, pp. 65–79. doi:https://doi.org/10.1016/j.actaastro.2016.03.030.
- [19] Maeda, T., Ozaki, T., Hara, S., and Matsui, S., “Touchdown Dynamics of Planetary Lander with Translation–Rotation Motion Conversion Mechanism,” *Journal of Spacecraft and Rockets*, Vol. 54, No. 4, 2017, pp. 973–980. doi:10.2514/1.A33630.
- [20] Kührt, E., Knollenberg, J., and Keller, H., “Physical risks of landing on a cometary nucleus,” *Planetary and Space Science*, Vol. 45, No. 6, 1997, pp. 665–680. doi:https://doi.org/10.1016/S0032-0633(96)00163-8.

- [21] Barbee, B. W., and Fowler, W. T., "Spacecraft mission design for the optimal impulsive deflection of hazardous Near-Earth Objects (NEOs) using nuclear explosive technology," *Planetary Defense Conference, Washington DC*, 2007.
- [22] Ulamec, S., and Biele, J., "Surface elements and landing strategies for small bodies missions – Philae and beyond," *Advances in Space Research*, Vol. 44, No. 7, 2009, pp. 847–858. doi:<https://doi.org/10.1016/j.asr.2009.06.009>.
- [23] Biele, J., Ulamec, S., Maibaum, M., Roll, R., Witte, L., Jurado, E., Muñoz, P., Arnold, W., Auster, H.-U., Casas, C., Faber, C., Fantinati, C., Finke, F., Fischer, H.-H., Geurts, K., Güttler, C., Heinisch, P., Herique, A., Hviid, S., Kargl, G., Knapmeyer, M., Knollenberg, J., Kofman, W., Kömle, N., Kührt, E., Lommatsch, V., Mottola, S., Pardo de Santayana, R., Remeteau, E., Scholten, F., Seidensticker, K. J., Sierks, H., and Spohn, T., "The landing(s) of Philae and inferences about comet surface mechanical properties," *Science*, Vol. 349, No. 6247, 2015. doi:[10.1126/science.aaa9816](https://doi.org/10.1126/science.aaa9816).
- [24] Otsuki, M., Baba, M., Satoh, Y., and Ishimura, K., "Landing Gear Team for the Martian Moons Exploration mission, Concept Study of Landing System of the Martian Moons Exploration Probe," *Proceedings of 61th Space Sciences and Technology Conference (in Japanese)*, 2017. JSASS-2017-4142-1G09.
- [25] Maeda, T., Otsuki, M., Baba, M., Imada, T., and Ishimura, K., "Landing Sampling and Takeoff Dynamics on Small Body with Fuel Sloshing," *Proceedings of 61th Space Sciences and Technology Conference (in Japanese)*, 2017. JSASS-2017-4383-2G13.
- [26] Ball, A., Garry, J., Lorenz, R., and Kerzhanovich, V., *Planetary Landers and Entry Probes*, Cambridge University Press, 2007. doi:[10.1017/CBO9780511536052](https://doi.org/10.1017/CBO9780511536052).
- [27] Rogers, W. F., "Apollo experience report: lunar module landing gear subsystem," 1972. NASA TN D-6850.
- [28] Desai, P. N., and Knocke, P. C., "Mars exploration rovers entry, descent, and landing trajectory analysis," *The Journal of the Astronautical Sciences*, Vol. 55, No. 3, 2007, pp. 311–323.
- [29] Cadogan, D., Sandy, C., and Grahne, M., "Development and evaluation of the mars pathfinder inflatable airbag landing system," *Acta Astronautica*, Vol. 50, No. 10, 2002, pp. 633–640. doi:[https://doi.org/10.1016/S0094-5765\(01\)00215-6](https://doi.org/10.1016/S0094-5765(01)00215-6).
- [30] Stein, J., Sandy, C., Wilson, D., Sharpe, G., and Knoll, C., "Recent Developments in Inflatable Airbag Impact Attenuation Systems for Mars Exploration," *44th AIAA/ASME/ASCE/AHS/ASC Structures, Structural Dynamics, and Materials Conference*, 2003. doi:[10.2514/6.2003-1900](https://doi.org/10.2514/6.2003-1900).
- [31] Do, S., de Weck, O., Jr., R. R., Pellicciotti, J., and Brady, T., "An Airbag-Based Crew Impact Attenuation System Concept for the Orion CEV - First Generation System Development," *AIAA SPACE 2009 Conference & Exposition*, 2009. doi:[10.2514/6.2009-6438](https://doi.org/10.2514/6.2009-6438).
- [32] Golombek, M. P., "The Mars Pathfinder Mission," *Journal of Geophysical Research: Planets*, Vol. 102, No. E2, 1997, pp. 3953–3965. doi:[10.1029/96JE02805](https://doi.org/10.1029/96JE02805).
- [33] Zeiner, H., French, C., and Howard, D., "A new approach to performance optimization of the 1975 Mars Viking lander," *Guidance and Control Conference*, 1973. doi:[10.2514/6.1973-889](https://doi.org/10.2514/6.1973-889).

- [34] Grover, M. R., Cichy, B. D., and Desai, P. N., "Overview of the Phoenix Entry, Descent, and Landing System Architecture," *Journal of Spacecraft and Rockets*, Vol. 48, No. 5, 2011, pp. 706–712. doi:10.2514/1.46548.
- [35] Prince, J. L., Desai, P. N., Queen, E. M., and Grover, M. R., "Mars Phoenix Entry, Descent, and Landing Simulation Design and Modeling Analysis," *Journal of Spacecraft and Rockets*, Vol. 48, No. 5, 2011, pp. 756–764. doi:10.2514/1.46561.
- [36] Ivanov, M. C., Blood, E. M., Cook, B. T., Giersch, L. R., Grover, M. R., Jakobowski, J. K., Rivellini, T. P., Su, R. P., Samareh, J. A., Zang, T. A., Winski, R. G., Olds, A. D., and Kinney, D. J., "Entry, descent and landing systems analysis study: Phase 2 report on Mars Science Laboratory improvement," 2011. NASA/TM-2011-216988.
- [37] Way, D., Davis, J., and Shidner, J. D., "Assessment of the Mars Science Laboratory entry, descent, and landing simulation," *Advances in the Astronautical Science*, Vol. 148, 2013, pp. 563–581.
- [38] Kornfeld, R. P., Prakash, R., Devereaux, A. S., Greco, M. E., Harmon, C. C., and Kipp, D. M., "Verification and Validation of the Mars Science Laboratory/Curiosity Rover Entry, Descent, and Landing System," *Journal of Spacecraft and Rockets*, Vol. 51, No. 4, 2014, pp. 1251–1269. doi:10.2514/1.A32680.
- [39] Steltzner, A. D., Miguel San Martin, A., Rivellini, T. P., Chen, A., and Kipp, D., "Mars Science Laboratory Entry, Descent, and Landing System Development Challenges," *Journal of Spacecraft and Rockets*, Vol. 51, No. 4, 2014, pp. 994–1003. doi:10.2514/1.A32866.
- [40] Northey, D., and Morgan, C., "Improved inflatable landing systems for low cost planetary landers," *Acta Astronautica*, Vol. 59, No. 8, 2006, pp. 726–733. doi:<https://doi.org/10.1016/j.actaastro.2005.07.058>.
- [41] Son, L., Kawachi, M., Matsuhisa, H., and Utsuno, H., "Reducing Floor Impact Vibration and Sound Using a Momentum Exchange Impact Damper," *Journal of System Design and Dynamics*, Vol. 1, No. 1, 2007, pp. 14–26. doi:10.1299/jsdd.1.14.
- [42] Yokoyama, T., and Higuchi, K., "Estimate of Impact Force at Landing on Lunar Surface by SPH Method," *Space Technology (in Japanese)*, Vol. 6, 2007, pp. 9–16. doi:10.2322/stj.6.9.
- [43] Maeda, T., Otsuki, M., and Hashimoto, T., "Overturning protection control of lunar-planetary lander with semi-active shock absorber," *Transactions of the JSME (in Japanese)*, Vol. 80, No. 816, 2014. doi:10.1299/transjsme.2014dr0235, dR0235.
- [44] MISUMI Corporation, <https://jp.misumi-ec.com/>, accessed 25/7/2018.
- [45] OptiTrack Japan, Ltd., <https://www.optitrack.co.jp/products/camera/flex13.html>, accessed 25/7/2018.
- [46] Satou, Y., Otsuki, S., Baba, M., Tobe, H., Ishimura, K., and Kitazono, K., "Compressive Behaviors of 3-D Additive Manufactured Truncated Octahedron for Impact Energy Absorption of Landing Gear," *Proceedings of 61th Space Sciences and Technology Conference (in Japanese)*, 2017. JSASS-2017-4356-2F07.
- [47] Christensen, E., Batterson, S., Benson, H., Choate, R., Hutton, R., Jaffe, L., Jones, R., Ko, H., Schmidt, F., Scott, R., et al., "Lunar surface mechanical properties," *Journal of Geophysical Research*, Vol. 73, No. 22, 1968, pp. 7169–7192.

- [48] Choate, R., Batterson, S. A., Christensen, E. M., Hutton, R. E., Jaffe, L. D., Jones, R. H., Ko, H. Y., Spencer, R. L., and Sperling, F. B., “Lunar surface mechanical properties,” *Journal of Geophysical Research (1896-1977)*, Vol. 74, No. 25, 1969, pp. 6149–6174. doi:10.1029/JB074i025p06149.
- [49] Hilchenbach, M., Küchemann, O., and Rosenbauer, H., “Impact on a comet: Rosetta Lander simulations,” *Planetary and Space Science*, Vol. 48, No. 5, 2000, pp. 361 – 369. doi:[https://doi.org/10.1016/S0032-0633\(00\)00011-8](https://doi.org/10.1016/S0032-0633(00)00011-8).